Theoretical investigations of chemically modified kesterites under strain

Inaugural Dissertation

to obtain the academic degree
Doctor rerum naturalium (Dr. rer. nat.)

submitted to
the Department of Biology, Chemistry, Pharmacy
of Freie Universität Berlin

by

Tim Küllmey
from Stendal
2021

This work was conducted under the supervision of

Prof. Dr. Beate Paulus (Freie Universität Berlin)

from August 2017 until August 2021

First reviewer:	Prof. Dr. Beate Paulus
Second reviewer:	Prof. Dr. Martin Lerch
Date of defense:	29.9.2021

Selbstständigkeitserklärung

Hiermit bestätige ich, dass ich die vorliegende Arbeit selbständig und nur unter Verwendung der angegebenen Literatur und Hilfsmittel erstellt habe. Außerdem versichere ich, dass diese Arbeit bei keinem früheren Promotionsverfahren eingereicht wurde.

Abstract

One of the most pressing issues of our time is to move away from fossil fuels to stop or limit global warming. One important technology which is used to replace energy from fossil fuels are photovoltaic solar cells. This thesis deals with a material class which can be used as a solar cell absorber called kesterites ($Cu_2ZnSnS_{4-x}Se_x$).
All commercially relevant solar cell absorber materials have certain drawbacks like high material usage and utilizing scarce or poisonous elements. Kesterite solar cells rely on abundant and relatively environmentally friendly elements. Furthermore kesterites have a high absorption coefficient for visible light which allows to use them in so called thin-film solar cells which are very efficient in terms of material usage. Kesterite solar cells are not yet matured to a level where they can compete commercially. Their biggest issue is a low conversion efficiency of the incoming solar energy. It stagnated at 13 % for the last 7 years while beyond 20 % conversion efficiency are required to be successful in the commercial market. One of the causes of the low conversion efficiency is that kesterites can easily get disordered, in particular Cu and Zn atoms which share a plane in the unit cell can interchange easily. Partly or fully replacing Cu and/or Zn with another cation can reduce the tendency to disorder. In this thesis we investigate unsubstituted kesterite (Cu_2ZnSnS_4) as well as various substituted variants.
In thin-films compressive stress can occur for various reasons, e.g. if a reactant is sputtered in the synthesis. We use first principle methods to scan for high pressure phase transitions for ordered and disordered kesterite and the following substituted variants: Cu_2FeSnS_4, Cu_2MnSnS_4, Ag_2ZnSnS_4 and Ag_2CdSnS_4. We investigate how the electronic structure changes through the structural phase transition. Cu_2CdSnS_4 has a different crystal structure than Cu_2ZnSnS_4. Using first principle methods we determine the maximum amount of Cd which can be used in Cu_2ZnSnS_4 to substitute Zn without changing the crystal structure.
For all investigated materials we predict a high pressure transition to a compressed rocksalt structure. The electronic structure of this high pressure phase is in all cases metallic which renders the materials useless as a solar cell absorber. The transition pressure for Cu_2ZnSnS_4 is predicted at 16 GPa, in excellent agreement with experimental results. The transition pressure for the substituted variants Cu_2FeSnS_4, Cu_2MnSnS_4 and Ag_2ZnSnS_4 are lower but still well off the pressures we expect in thin-film synthesis. Only the transition pressure for Ag_2CdSnS_4 which is 4.7 GPa is close to pressures which can occur in thin-films. Therefore we advice to monitore the structure if this material is used as a solar cell absorber. For the solid solution series $Cu_2Cd_xZn_{1-x}SnS_4$ we predict the kesterite-type structure to be most stable up to Cd_x=0.51. Experimentally it is most stable up to Cd_x=0.40. We show that the difference may be due to a small disorder in the experimental samples.

Kurzzusammenfassung

Einer der wichtigsten Herausforderungen unsere Zeit ist es, die Nutzung fossiler Energieträger zugunsten erneuerbarer Energieträger einzustellen, um die globale Erwärmung zu stoppen beziehungsweise zu limitieren. Eine wichtige Technologie für eine nachhaltigen Energieversorgung ist die Photovoltaik. Diese Arbeit beschäftigt sich mit einer Klasse von Materialen, die als Absorber in Solarzellen eingesetzt werden können, den sogenannten Kästeriten ($Cu_2ZnSnS_{4-x}Se_x$).
Alle kommerziell relevanten Absorbermaterialien haben gewisse Nachteile, wie einen hohen Materialverbrauch oder die Nutzung von seltenen oder giftigen Elementen. Kästerite bestehen aus nicht-giftigen Elementen, die auf der Erde leicht verfügbar sind. Außerdem haben Kästerite einen hohen Absorptionskoeffizienten für sichtbares Licht, was sogenannten Dünnschichtsolarzellen ermöglicht, die besonders wenig Material benötigen. Kästeritsolarzellen sind technologisch noch nicht so ausgereift, dass sie kommerziell relevant sind. Das größte Problem ist eine zu kleine Effizienz bei der Umwandlung der Solarenergie. Diese Effizient stagniert seit sieben Jahren bei 13 %, während mehr als 20 % nötig sind um am Markt bestehen zu können. Einer der Gründe für die niedrige Effizienz ist, dass Kästerite anfällig für Unordnung sind. Speziell Cu- und Zn-Atome, welche sich eine Ebene in der Einheitszelle teilen, können leicht ihre Plätze tauschen. Indem man Cu und/oder Zn vollständig oder teilweise durch andere Kationen ersetzt, kann man die Neigung zur Unordnung reduzieren. In dieser Arbeit beschäftigen wir uns mit unsubstituiertem Kästerit (Cu_2ZnSnS_4) und einigen substituierten Varianten.
In Dünnschichten kann es zu Druckspannung kommen, z.B. wenn ein Reaktant in der Synthese gesputtert wird. Wir benutzen First-principle-Methoden um nach Hochdruckphasenübergängen für geordnetes und ungeordnetes Kästerite und für folgende substituierte Varianten zu suchen: Cu_2FeSnS_4, Cu_2MnSnS_4, Ag_2ZnSnS_4 und Ag_2CdSnS_4. Wir untersuchen dabei auch, wie sich die elektronische Struktur durch den Phasenübergang verändert. Cu_2CdSnS_4 hat eine andere Kristallstruktur als Cu_2ZnSnS_4. Mittels First-principle-Methoden bestimmen wir den maximalen Anteil an Cd, der substituiert werden kann, ohne dass sich die Kristallstruktur ändert.
Für alle untersuchten Materialien sagen wir einen Hochdruckphasenübergang zu einer gestauchten Kochsalz-Struktur voraus. Dabei ist die Hochdruckphase immer metallisch, wodurch das Material als Solarzellenabsorber unbrauchbar wird. Der übergangsdruck für Cu_2ZnSnS_4 ist 16 GPa, was in sehr guter Übereinstimmung zum Experiment steht. Die Übergangsdrücke für die substituierten Varianten Cu_2FeSnS_4, Cu_2MnSnS_4 und Ag_2ZnSnS_4 sind niedriger, allerdings immer noch deutlich über Drücken, die in Dünnschichten zu erwarten sind. Nur der Übergangsdruck von 4.7. GPa für Ag_2CdSnS_4 ist im Bereich der Drücke, die in Dünnschichten auftreten. Für den Mischkristall $Cu_2Cd_xZn_{1-x}SnS_4$ sagen wir voraus, dass die Kästerit-Struktur bis zu Cd_x=0.51 am stabilsten ist. Experimentell liegt die Struktur bis Cd_x=0.40 vor. Wir zeigen, dass die Differenz durch kleine Unordnungen in den experimentellen Proben zu erklären sein könnte.

List of publications

Paper A

"Pressure-induced structural and electronic transitions in kesterite-type Cu_2ZnSnS_4"

Efthimiopoulos, I., Küllmey, T., Speziale, S., Pakhomova, A. S., Quennet, M., Paulus, B., Ritscher, A., Lerch, M. and Koch-Müller, M., *J. Appl. Phys.* **2018**, *124*(8), 085905
DOI: 10.1063/1.5047842

Paper B

"High-pressure behavior of disordered kesterite-type Cu_2ZnSnS_4"

Efthimiopoulos, I., Küllmey, T., Speziale, S., Pakhomova, A. S., Quennet, M., Paulus, B., Ritscher and A., Lerch, M., *Appl. Phys. A* **2021**, *127*, 616
DOI: 10.1007/s00339-021-04745-w

Paper C

"Calculation for high pressure behaviour of potential solar cell materials Cu_2FeSnS_4 and Cu_2MnSnS_4"

Küllmey, T., González, M., Heppke, E. M. and Paulus, B., *Crystals* **2021**, *11*(2), 1–19
DOI: 10.3390/cryst11020151

Paper D

"High pressure behavior and disorder for Ag_2ZnSnS_4 and Ag_2CdSnS_4"

Küllmey, T., Hein, J., Heppke, E. M., Efthymiopoulos, I. and Paulus, B., manuscript will be submitted to *ACS Omega* with minor changes

Paper E

"Experimental and theoretical investigations on the composition-dependent structural phase transition in $Cu_2Cd_xZn_{1-x}SnS_4$"

Heppke, E. M., Küllmey, T., Efthimiopoulos, I., Avci, F. D., Appelt, O., Paulus, B. and Lerch, M., *Mater. Res. Express* **2019**, *6*(12), 1125525
DOI: 10.1088/2053-1591/ab59a0

Contents

List of Figures

List of Tables

1 Introduction

1.1 Motivation: solar cells

In the light of global warming, one of the most pressing issues is to move away from fossil energy sources to prevent the production of more CO_2 driving the greenhouse effect. The total average power available at the earth's surface in the form of solar radiation exceeds the total human power consumption by roughly a factor of 1,500.[3] Of course it is not feasible to access all of that power but the number shows that there is a lot of potential in using solar power. Still there are many challenges in using solar power, like the fact that the highest power of solar energy tends to be available in regions with a small population density like deserts and that it is still a big challenge to store and transport electrical energy. Nevertheless it is widely recognized that solar power is one of the fundamental building blocks to create a sustainable energy supply for the whole world. One key technology to exploit solar radiation for energy production are solar cells which will be briefly explained in the following.

1.1.1 Principle

In solar cells the aim is the conversion of energy from solar radiation to electrical energy. To demonstrate the physical principle of solar cells we use the pn junction (fig. 1.1) which is realized in commercial silicone based solar cells. It consists of two adjoint semiconductors, one of them being p-type and the other one being n-type. A p-type semiconductor has an access of holes (which are missing electrons), an n-type semiconductor has an access of electrons. Both types can be produced by doping, which refers to replacing a small amount of atoms of the semiconductor base material with dopant atoms which have more (n-type) or less valence electrons (p-type) than the atoms they replace. For silicone phosphorus (n-type) and boron (p-type) are typically used for doping. The energy of the electron bound to the dopant in n-type doping is only slightly smaller than the lower edge of the conduction band (fig. 1.2). The n-type dopants therefore donate their electrons easily to the conduction band. The energy of an electron of the dopant in p-type doping is only slightly greater than the upper edge of the valence band. Therefore it accepts an electron easily from the valence band.

Where n- and p-type semiconductors are joined the electrons and holes recombine leaving behind two ionic zones. Both zones together are called depletion region (fig. 1.1) because we find neither electron nor holes in this region. In the n-type zone of the depletion region the

remaining ionic charge is positive and in the p-type zone it is negative. This gives rise to an electric field pointing from the n-type to the p-type semiconductor. If light with at least the band gap energy penetrates the depletion region the photon is absorbed and an electron hole pair is formed. The electric field accelerates electron and hole in opposite directions towards the electrodes. Electrons accumulate in the n-type semiconductor and holes in the p-type semiconductor, giving rise to a potential difference. If both electrodes are connected through a consumer an electric current is observed, the electrons travel through the consumer to the positive electrode to recombine with the holes. Thus electrical energy is generated.

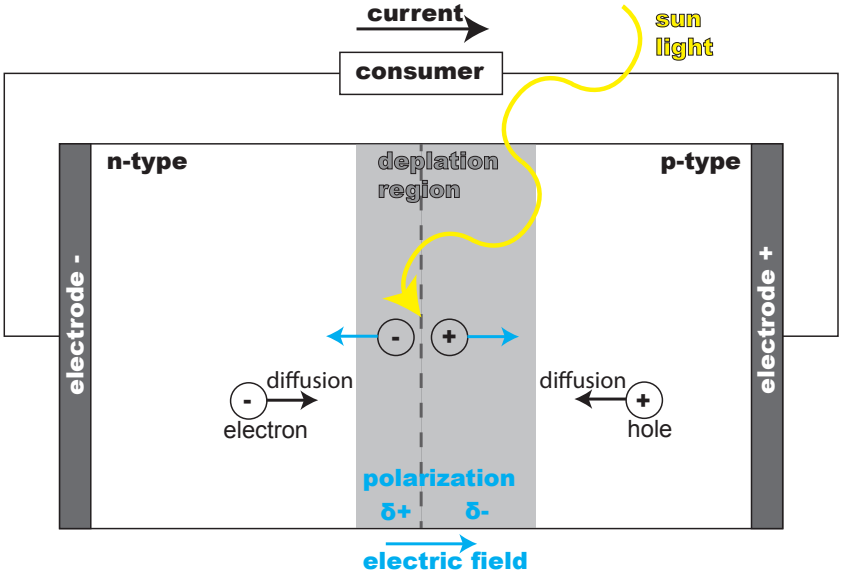

Figure 1.1: Schematic illustration of a pn junction used as a solar cell. Absorption of solar radiation induces the electron hole pair formation in the pn junction, then the electron and hole are transported to the negative and positive electrode, respectively generating a current which is used by the consumer.

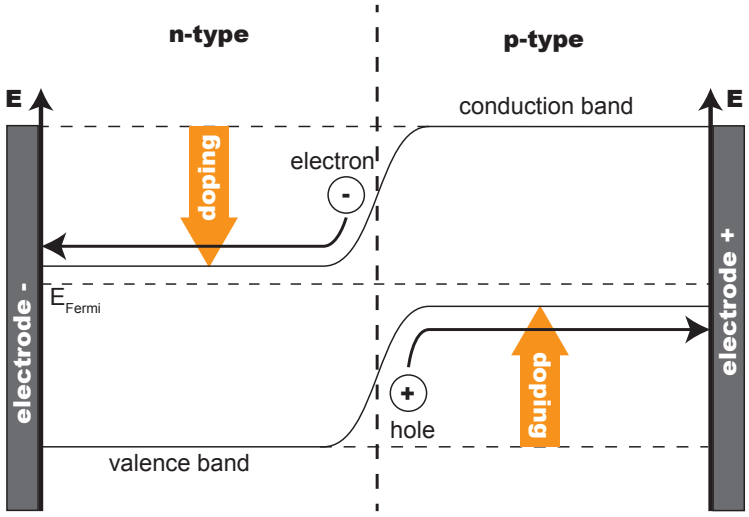

Figure 1.2: Schematic illustration of band diagram of a pn junction for the same semiconductor base material, e.g. silicone with phosphorus (n-type) and boron (p-type) doping. Doping shifts the valence and conduction bands as indicated by the orange arrows.

The electric field in the depletion region makes it less likely that the electron and holes recombine. It is not the only driving force for the charge carriers though, there is also a diffusion gradient in the opposite direction. That is due to the lack of holes on the n-type side and the lack of electrons in the p-type side. The reason why electrons only reach the negative electrode is that the p-type material outside the depletion region acts as a membrane which can only be penetrated by holes because electrons immediately recombine with the access of holes. Also holes can only reach the positive electrode because the n-type material outside the depletion regions acts as a membrane which only allows for the conduction of electrons as holes immediately recombine.

Important parameters to characterize solar cells are the open circuit potential V_{OC}, short circuit current (I_{SC}), fill factor (FF) and the conversion efficiency η.[4] V_{OC} is the potential difference of the two electrodes under illumination, it is proportional to the band gap. I_{SC} is the maximum current measured under illumination if the two electrodes are short circuited. To remove the dependence of the solar cell area, usually the short-circuit current density (J_{SC} in $\frac{mA}{cm^2}$) is listed rather than the short-circuit current. The fill factor is the quotient of the experimentally measured maximum power of the cell under illumination P_{max} and the theoretical maximum power given by $I_{SC} \cdot V_{OC}$:

$$FF = \frac{P_{max}}{V_{OC} \cdot I_{SC}} = \frac{V_{max} \cdot I_{max}}{V_{OC} \cdot I_{SC}} \ . \tag{1.1}$$

The conversion efficiency η is the fraction of solar radiation power incident on the unit area P_{in} recovered by the solar cell:

$$\eta = \frac{P_{max}}{P_{in}} = \frac{V_{max} \cdot I_{max}}{P_{in}} \ . \tag{1.2}$$

1.1.2 *Shockley-Queisser*-limit

The upper limit of the conversion efficiency of solar cells was predicted in 1961 by *Shockley* and *Queisser*.[5] Initially the paper was not recognized by their peers but their paper has evolved to become one of the most cited paper in the field of solar cells. It is still considered valid for conventional pn junctions like Si based solar cells. Nevertheless the *Shockley-Queisser*-limit has been beaten in 2013 using an organic material where one photon induces two instead of one electron hole pairs by Singlet-Exciton-Fission.[6]

Shockley and *Queisser* took a thermodynamical approach, applying the principle of detailed balance to solar cells. The general idea is to calculate the absorption flux and the flux emitted from the solar cell. The difference between the two fluxes (multiplied by the charge) is the maximum current from the solar cell. The sun and the solar cell itself are regarded as black bodies at different temperatures, the absorption of all photons with more energy than the band

gap of the semiconductor is assumed to be complete, furthermore the transport of electrons and holes within the semiconductor is assumed to be lossless. The only considered mechanism of energy loss from the cell is radiative recombination. The limit depends on multiple factors, most importantly the band gap and the temperature of the solar cell material. At 300 K the maximum efficiency is 30 % at 1.2 eV band gap (fig. 1.3). For comparison, commercial crystalline single junction silicon solar cells reach about 20% efficiency, the record efficiency is currently at 26 %.[7]

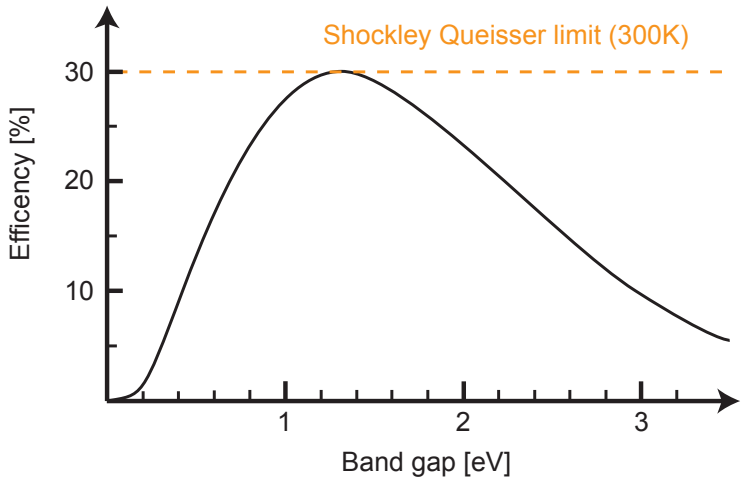

Figure 1.3: Efficiency of solar cells with radiative recombination only (as assumed for the *Shockley-Queisser*-limit) as a function of their band gap. Adapted from literature.[8]

1.1.3 Thin-film solar cell technologies

The solar market is dominated by polycrystalline silicon cells. Their largest disadvantage is that they are not efficient. The reason is that silicone has a low absorption coefficient for visible light which makes a high absorber thicknesses necessary. One trend emerging are thin-film solar cells, they work with absorber thicknesses of about 1-2 µm, while regular cells have absorber thicknesses of 200 µm. To have effective thin-film cells the absorber must have a very high absorption coefficient. Using thin-films has some advantages, the most obvious being that much less material is used. From that follows a lower energy payback time, which is the time it takes to recover the energy needed for the production of the solar cell itself. By now the module prices of thin-film cells have become comparable to polycrystalline silicon cells for some technologies despite the much lower production volume. Another advantage of thin-films as absorbers is that they can be extended to flexible substrates, which enables completely new applications. It is expected that in the long term, thin-film photovoltaic technology will surpass crystalline technologies in the mass market. However, low-cost manufacturing and rising efficiencies of crystalline silicon technologies led to a declining demand for thin-film technologies in the past five years.[9]

In the following we will briefly introduce the commercially established thin-film solar cell technologies. The first and oldest technology is amorphous silicon, or α-Si. The first cell was built in 1976 by *Carlson* and *Wronski*.[1] They used hydrogenated α-Si, in the following referred to as α-Si:H. The hydrogenation passivates dangling bonds which otherwise lead to unwanted recombination reactions. α-Si:H is transparent up to 1.7 eV and starts to be highly absorptive at 2 eV. The direct optical band gap is 1.75 eV. The first working α-Si:H cell (fig. 1.14) was coated on a glass substrate. The first layer is transparent and conducting indium tin oxide serving as the positive front contact. The pn junction of a crystalline Si solar cell is extended to a pin junction, where between p and n region an intrinsic region is placed. As in crystal silicon the n layer is doped with phosphorous and the p layer is doped with boron. The intrinsic region which is thicker than the other two is only very slightly doped with boron. The intrinsic region is flooded with charge carriers from the p and n region where they recombine, leaving behind a much larger depletion region than in the pn junction, described above. Due to the larger depletion region the separation of the charge carriers is improved in comparison to a pn junction. At the back of the cell another layer of indium tin oxide and the silver back contact follow. The first α-Si:H cell achieved an efficiency of 2.4 %. Many technical advances like using multi junctions, tuning the band gap by incorporating germanium and incorporating a metal reflector have lead to a record efficiency of 14.0 % in 2016.[10]

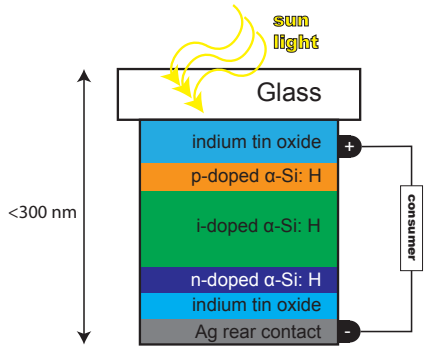

Figure 1.4: Schematic drawing of first α-Si solar (p-i-n) cell as built in 1976 by *Carlson* and *Wronski*.[1], drawing adapted from literature.[9]

The commercially most successful thin-film solar cell material at the moment is CdTe. CdTe is a semiconductor with a direct band gap of 1.44 eV. It adopts a cubic crystal structure with tetrahedral coordination for all atoms (fig. 1.5). In the CdTe solar cell (fig. 1.6) it is used as p-doped absorber layer in a pn CdTe-CdS hetero junction. The pn junction is coated onto glass with a conducting transparent tin oxide layer on top, followed by a metal (e.g. Mo) rear contact.

CdTe cells can reach high efficiencies beyond 20 %, with a current world record of 22.4 %.[7] The high efficiency and the simple cell design enable cells as cost effective or even better than crystal silicone. The challenges with CdTe technology are a shorter life time than Si based cells, furthermore the toxicity of Cd is concerning and it is unclear if there is enough Te available to replace Si cells in the mass market.

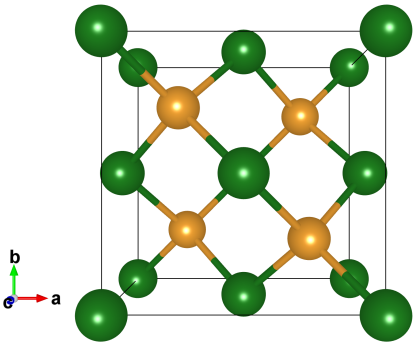

Figure 1.5: CdTe with its cubic crystal structure (SG: $F\bar{4}3m$) with indication of bonds between cations and anions. Green: Cd, orange: Te.

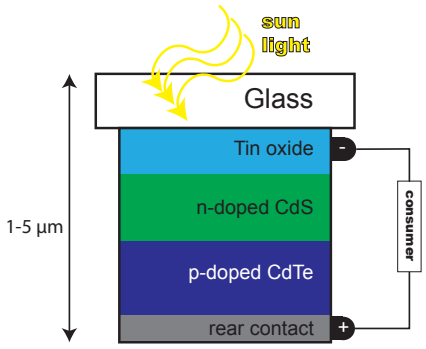

Figure 1.6: Schematic drawing of CdTe solar cell. Adapted from literature.[11]

Copper indium gallium selenide (CIGS) solar cells have a direct optical band gap of 1 to 1.7 eV. The absorber material has varying compositions, it can be constructed from a solution series of $CuInSe_2$ where Indium is partly replaced with Gallium: $CuIn_{1-x}Ga_xSe_2$. The absorber material has a chalcopyrite-type structure (SG: $I\bar{4}2d$, fig. 1.7). The band gap is tuned by varying x. For x equals 0, the band gap of the material is 1.0 eV and for x equals 1, it is 1.7 eV. The absorber material is used in its p-doped variant, forming a pn heterojunction with n-type CdS. The pn junction is deposited on top of a Mo rear contact on a glass substrate (fig. 1.8). Mo films have been widely adopted as back contacts for CIGS solar cells because they are stable at high processing temperatures and resistant to alloying with Cu, also they exhibit excellent adhesion between the soda lime glass substrates and CIGS absorbers and they present a low-resistance contact to the CIGS absorber.[12] On top an intrinsic ZnO layer followed by the transparent conducting front contact made of n-doped ZnO is added.

CIGS cells reach high efficiencies at a relatively low cost. The lab scale record is 23.3 %. The main problems of this technology are that In and Ga are scarce elements and it is questionable if there is enough supply to replace silicone cells in the mass market.

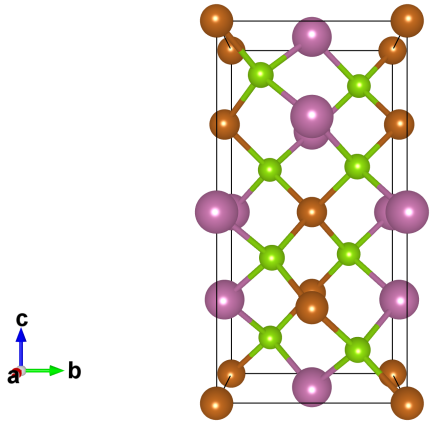

Figure 1.7: $CuInSe_2$ with its tetragonal crystal structure (SG: $I\bar{4}2d$) with indication of bonds between cations and anions. Copper: Cu, light purple: In, light green: Se.

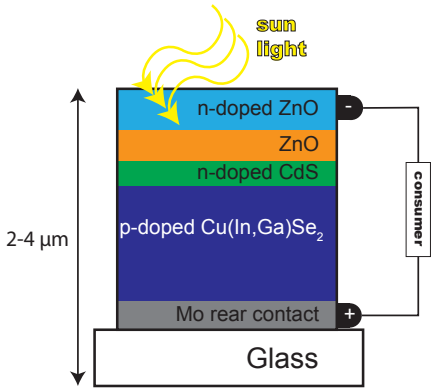

Figure 1.8: Schematic drawing of CIGS solar cell. Adapted from literature.[9]

1.2 Kesterite-type semiconductor thin-film solar cells

In 1997[13] a different chalcopyrite-based semiconductor material was tested for solar absorbers in an effort to overcome the shortcomings of CIGS and CdTe solar cells, namely the scarcity of In and Ga and the toxicity of Cd and Se. The material is called kesterite named after a mineral with the ideal sum formula Cu_2ZnSnS_4 (CZTS). The choice was inspired by CIGS absorbers, if we replace one half of the In in $CuInSe_2$ (fig. 1.7) with Zn and the other half with Sn, we end up with the kesterite-type structure (fig. 1.9).[14] It has an almost optimal bandgap (E_g=1.5 eV, measured optical band gap[15]) and a high absorption coefficient in the visible energy range which is beneficial for the use as an absorber material and it consists of earth-abundant, low-cost, and relatively environmentally friendly elements.[15,16] Besides the CZTS sulfide, also the selenide $Cu_2ZnSnSe_4$ (CZTSe, E_g=1.0 eV) and the solution series $Cu_2ZnSnS_{4-x}Se_x$ (CZTSSe) adopt a kesterite-type structure and therefore also belong to the family of kesterite materials.[17] The band gap can be tuned between 1.5 eV (x=0) and 1.0 eV (x=4) manipulating the S/Se ratio in the solution series CZTSSe.[18] The cell design itself (fig. 1.10) has been adopted from the CIGS solar cell. Typically it consists of an Mo rear contact coated on soda lime glass, followed by the p-type CZTS(e) absorber, n-doped CdS, and a ZnO window. MgF_2 may be added as an anti reflection coating. CZTS(e) shows natural p-type conductivity due to intrinsic doping by Cu vacancies and Cu_{Zn} anti sites.[15] The Mo back contact has been adopted from CIGS cells. The CZTS(e)/Mo interface is thermodynamically unstable,[19] the resulting formation of secondary phases (mostly $MoS(e)_2$) at the back contact reduces the efficiency.[20]

The first cell only had an efficiency of 0.66 %[13]. In the following 20 years of research numerous advances have been made, the current record efficiency is 12.6 % achieved in 2014.[21] One very important insight is that all high performing kesterites are off-stoichiometric. Therefore

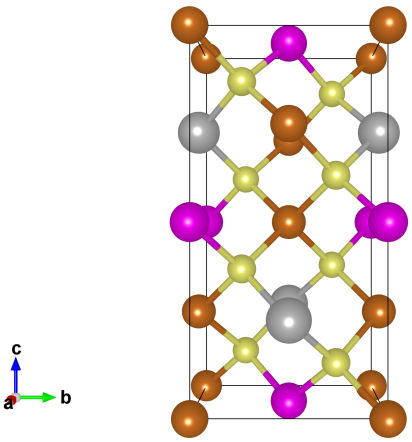

Figure 1.9: Cu_2ZnSnS_4 with its tetragonal crystal structure (SG: $I\bar{4}$) with indication of bonds between cations and anions. Copper: Cu, pink: Zn, grey: Sn, yellow: S.

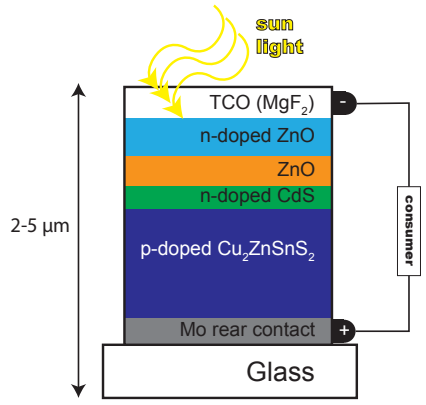

Figure 1.10: Schematic drawing of CZTS solar cell. Adapted from literature.[4]

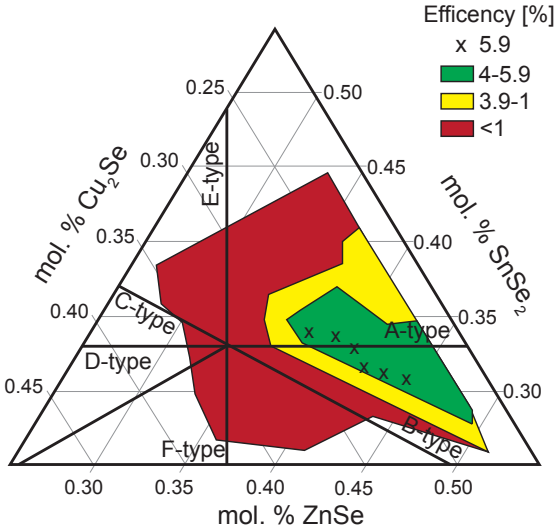

Figure 1.11: Compositional dependence of $Cu_2ZnSnSe_4$ device efficiency shown in a pseudo-ternary phase diagram of Cu_2Se–ZnSe–$SnSe_2$. Adapted from literature.[24]

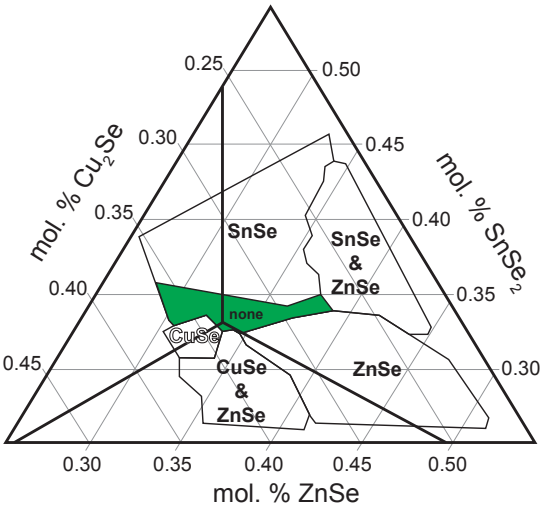

Figure 1.12: Compositional dependence of $Cu_2ZnSnSe_4$ secondary phases shown in a pseudo-ternary phase diagram of Cu_2Se–ZnSe–$SnSe_2$. Adapted from literature.[24]

Lafond et al.[22] and later *Gurieva et al.*[23] classified different off-stoichiometric CZTS(e) compositions each of them corresponding to different cationic balances, combining all possible poor and rich regions for each cation. They labeled the different compositions with letters from A to M. *Dimitrievska et al.* systematically tested 200 off-stoichiometric compositions with regard to their efficiency in a solar cell (fig. 1.11).[24] It strikes that the high performing materials are close to the A-line which is Cu-poor, Zn-rich, Sn-stoichometric.

The reason why Zn rich conditions are necessary is thought to be found in the reaction mechanism. The direct reaction of metals with the chalcogenide to form kesterite is almost

impossible, as at least the ZnS(e) phase is more stable than the quaternary phase, and it is therefore expected that simpler binary and/or ternary chalcogenide species are formed first. Depending on the reaction conditions the chalcogenide species react via one of the following reactions to form kesterite:[17]

$$Cu_2S(e) + ZnS(e) + SnS(e) + \frac{1}{2}S(e)_2 \longleftrightarrow Cu_2ZnSnS(e)_4 \tag{1.3}$$

$$Cu_2SnS(e)_3 + ZnS(e) \longleftrightarrow Cu_2ZnSnS(e)_4 \ . \tag{1.4}$$

Regardless of the mechanism, ZnS(e) is formed first. If initially the composition is Zn-stoichometric this leads to Zn-poor conditions for the kesterite forming reaction (eq. 1.3 or 1.4). Under those conditions detrimental Zn point defects are formed.[24] This can be avoided initially using Zn rich conditions. Cu-poor conditions are favored because they lead to the required p-type conductivity, which is promoted by V_{Cu} vacancies. All defects forming under Cu-poor conditions are shallow defects which should have a limited impact on recombination processes.[25]

Many approaches have been tested to fabricate kesterite solar cell devices: sputtering (η_{max}= 8.1 %[26]), evaporation (η_{max}= 11.6 %[27]), solution-based approach (η_{max}= 12.6 %[21]), electro-deposition (η_{max}= 8.2 %[28]) and metallurgy (η_{max}= 5.9 %[29]). Regardless of the preparation method the highest-performing kesterite absorber materials are post reaction annealed in $H_2S(e)$ atmosphere. Typical annealing temperatures are 500°C to 600°C with annealing times from 5 minutes to 3h.[20] To ensure the stabilization of the thermodynamically favored crystal structures with as little defects as possible samples are in some cases cooled at a controlled slow rate, e.g. 60K/h.[30] The annealing leads to a significant improvement in grain size and morphology of the CZTS(e) thin-film.[31] The $H_2S(e)$ atmosphere suppresses decomposition of the kesterite absorber at the kesterite absorber/Mo interface.[12] The supply of S/Se ensures that Mo reacts with gaseous S/Se and not the CZTSSe absorber to form $MoSe_2$, minimizing the formation of undesirable secondary phases within the absorber.[19]

The CZTS top efficiency cell (η= 12.6 %[21]) has a band gap of 1.13 eV. For this band gap the *Shockley-Queisser* limits for V_{OC}, J_{SC}, FF and η are 820mV, 43.4 $\frac{mA}{cm^2}$, 0.871 and 31 %, respectively. The CZTSSe record cell only achieved a V_{OC} of 513.4 mV, a J_{SC} of 35.2 $\frac{mA}{cm^2}$ and a FF of 0.698, corresponding to 62.6 %, 81.1 % and 80.1 % of the *Shockley-Queisser* limit values, respectively.[21] A high performing (η= 20 %) CIGS cell with nearly the same band gap (1.14 eV) reaches a V_{OC} of 730 mV, a J_{SC} of 35.7 $\frac{mA}{cm^2}$ and a FF of 0.777.[32] This comparison shows the biggest issue with CZTS(e) solar cells, a large deficit in V_{OC}, and also a smaller deficit in FF while J_{SC} is comparable to the high performing CIGS cell. A deficit in V_{OC} means that a significant amount of charge carriers recombine before reaching the electrodes.

The reasons for the V_{OC} deficit are still not fully understood. I will present the four most relevant areas which are discussed in the kesterite research community to improve V_{OC}.

Firstly, it is suspected that interface recombination at the CdS/CZTS(e) interface contributes to the V_{OC} deficit. The band alignment at the interface is important, the difference in energy between the CdS conduction band and the p-type absorber conduction band is called conduction band offset (CBO, fig. 1.13). For CIGS the optimal CBO is between 0 and 0.4 eV. Values below 0 lead to increased interface recombination via interface defects while values above 0.4 eV lead to a barrier which is increasingly harder to pass for the electrons, significantly reducing the efficiency. There are contradictory results regarding the CBO in CZTSSe solar cells. *Haight et al.* noted a CBO of about 0.5 eV at the CZTSSe/CdS interface of solution processed CZTSSe for all values of $\frac{[S]}{[S+Se]}$ they tested.[33] *Bär et al.* measured a CBO of -0.33 eV for co-evaporated CZTS.[34] The different results may result from the different composition of materials at the CZTSSe surface, because of different sample and surface preparation methods, which modify the interface band structure.[12] Further testing and optimization is necessary to ensure minimal interface recombination. From an environmental point of view it is desirable to replace the CdS buffer layer with a non toxic material like ZnS[19] or In_2S_3.[35]

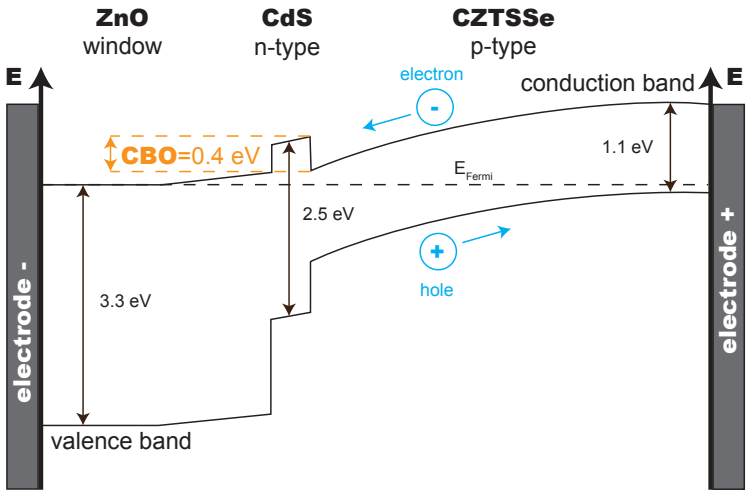

Figure 1.13: Schematic illustration of ideal band diagram of a CZTSSe solar cell. The conduction band offset (CBO) is highlighted in orange.

Secondly, part of the V_{OC} deficit is expected to be due to bulk recombinations. One cause for those are bulk inhomogeneities caused by secondary phases. It is challenging to control the chemical composition of kesterite materials within the copper-poor and zinc-rich chemical potential window while avoiding the formation of secondary phases, because phase pure kesterite has a narrow phase stability region.[12] E.g. close to the A-line the formation of ZnS(e) is likely (fig. 1.12). Another cause for bulk recombinations are deep defects. In CZTSSe those are Sn_{Zn} and Zn_{Sn} anti sites, Sn vacancies and possibly reduced Sn species.[17]

Thirdly, one of the principle causes of the V_{OC} deficit is thought to be band tailing. Band tail states are localized electronic states existing just below the conduction band or right above the valence band.[36] Consequently if band tailing states are present the band gap gets reduced. Band tailing has been noted in even the highest performing devices. In comparison to CIGS absorbers CZTSSe suffers from significantly more band tailing.[37] Band tailing is typically observed for disordered structures. The kesterite structure can easily be disordered because Cu_{Zn} Zn_{Cu} anti sites have a low energy of formation.[38] They form in the *a*-*b* planes Cu^+ and Zn^{2+} occupy (fig. 1.9). The exchange is promoted by the similar ionic radii of Cu^+ (r=0.60 Å[39]) and Zn^{2+} (r=0.60 Å[39]). PBE calculations show that clustering of [Cu_{Zn}+Zn_{Cu}] pairs is favorable and that their density is sufficient to cause a significant reduction of the effective band gap. Disorder will introduce spatial band gap fluctuations in the range of several 100 meV.[40,41] Another effect which is discussed as the cause of band tailing is fluctuations in the electrostatic potential also caused by the Cu-Zn disorder.[38] Either way controlling and avoiding disorder in CZTSSe devices is one of the major challenges towards more efficient kesterite solar cells.

Fourthly, the Mo/CZTS(e) interface at the back contact needs to be improved. CZTS(e) reacts with Mo in a thermodynamically favorable reaction to form $MoS(e)_2$, $Cu_2S(e)$, ZnS(e), and SnS(e).[19] Those secondary phases increase the resistance of the back contact and reduce the efficiency. An alternative back contact material that can withstand the full device processing and maintain low series resistance needs to be engineered.[9]

For CTZSSe to become a commercially relevant thin-film photovoltaic material it needs to clearly outperform α-Si cells and become similarly efficient as CIGS and CdTe cells. If we compare the historic development of efficiencies of CTZSe to the commercial thin-film technologies (fig. 1.14) it strikes that CZTSe research started 20 years after the other technologies. The initial slope in the first 20 years for CZTSe is comparable to the other three technologies. If we assume that the future developments in CZTSe will be comparable to the developments for CIGS and CdTe technology, we can expect CZTS cells with +20 % efficiency in 20-40 years. The time may also be reduced because of the larger knowledge and better simulation tools in comparison to the past when CIGS and CdTe technology were developed.

The proposed strategies to advance towards more efficient CZTS(e) solar cells are doping and alloying with isoelectric elements and with alkali elements.[17] The primary goal is to reduce the V_{OC} deficit. Cu can be partly replaced by Ag (r=1.00 Å[39]) to reduce the band tailing associated to Cu-Zn disorder. Zn can be replaced by Cd, Mn, Mg, Fe. This is also expected to reduce the tendency to disorder but also improve bulk homogeneity as the particularly stable secondary phase ZnS can not be formed. Furthermore, the deep Zn_{Sn} defect can be avoided. Similarly Sn can be replaced by Ge to avoid the Sn_{Zn} deep defect. Another important point is to improve the synthesis process to ensure phase pure KS with large grains. For that purpose Li, Na and K doping are tested with good results, especially for Li.[42]

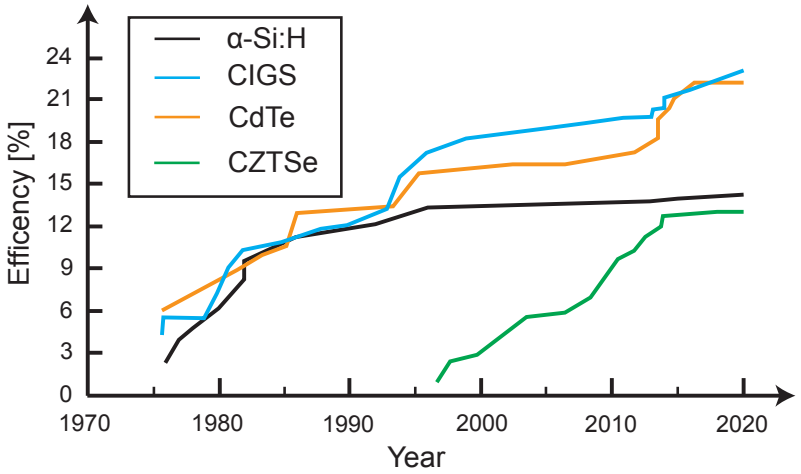

Figure 1.14: Development of the efficiencies of α-Si: H, CdTe, CIGS and CZTSe solar cells from 1970 until now. Plot adapted from literature.[9,17]

1.3 Scope of this work

In this work we probe the effect of compressive stress to CZTS and certain cation substituted variants. Compressive stress is of importance for the use as thin-film solar cells especially if their synthesis involves sputtering. The ion bombardment in the sputtering deposition leads to compressive stress.[43,44] In CZTSSe solar cells either the absorber material itself is sputtered[45] or the buffer layer CdS, the transparent conducting oxide ZnO and the antireflection coating MgF_2 layer on top are sputtered.[21] Besides Cu_2ZnSnS_4, we chose to study Ag_2ZnSnS_4, Ag_2CdSnS_4, Cu_2MnSnS_4 and Cu_2FeSnS_4 with regard to their high-pressure behavior. All those substitutions are discussed in the context of improving the V_{OC} deficit of CTZSSe. Furthermore, we study the stability of disordered structures for Ag_2ZnSnS_4 and Ag_2CdSnS_4. Finally we investigate the solution series $Cu_2Zn_{1-x}Cd_xSnS_4$. Cu_2ZnSnS_4 has a KS structure while Cu_2CdSnS_4 has a different crystal structure. We aim to determine the Cd substitution fraction x_{Cd} where the structure flips because this presents the maximum x_{Cd} substitution fraction for doping of CTZS without losing the KS structure.

The high-pressure study on Cu_2ZnSnS_4 was carried in collaboration with AG Lerch (TU Berlin) who synthesized the samples and Dr. Ilias Efthymiopoulos (GeoForschungsZentrum Potsdam, Universität Greifswald) who supervised the high-pressure X-ray diffraction (XRD) experiments. Our collaborators at AG Lerch conducted XRD experiments to analyze the phase transition in $Cu_2Zn_{1-x}Cd_xSnS_4$. The high-pressure studies on Ag_2ZnSnS_4, Ag_2CdSnS_4, Cu_2MnSnS_4 and Cu_2FeSnS_4 were carried out purely theoretically.

To address the research questions above we carried out first principle calculations at the PBE[46] level to determine equilibrium structures of KS, certain substituted variants and the solution series $Cu_2Zn_{1-x}Cd_xSnS_4$. In the high-pressure projects we furthermore calculated PBE enthalpies as a function of pressure. Additionally we calculated PBE enthalpies for potential

high-pressure phases which enables us to predict high-pressure phase transitions of the materials. We also analyzed the evolution of the electronic structure during the high-pressure phase transition using the HSE06 [47] hybrid functional.

2 Theoretical background

2.1 Electronic structure

2.1.1 *Hartree-Fock* (HF) theory

In 1926 *Schrödinger* introduced the idea that particles can be fully described by a wave function which is the foundation of the field of quantum mechanics. He introduced the time-dependent *Schrödinger* equation:[48]

$$\hat{H}\Phi_j(t) = i\hbar\frac{\partial}{\partial t}\Phi_j(t) \ . \tag{2.1}$$

It contains the Hamilton operator $\hat{H}$, the time-dependent wave function $\Phi_j(t)$ of the state j, the time t, the imaginary unit i and the reduced Planck constant $\hbar$. The calculation of many material properties like (crystal) structures or excitation energies (band gaps) do not require a time-dependent treatment. To describe those properties the stationary *Schrödinger* equation, written in atomic units using the electronic structure Hamiltonian, suffices:

$$\begin{aligned}
\hat{H}\Psi_j &= (\hat{T}_e + \hat{T}_n + \hat{V}_{en} + \hat{V}_{ee} + \hat{V}_{nn})\Psi_j && (2.2)\\
&= \left(-\sum_{i=1}^{N}\frac{1}{2}\nabla_i^2 - \sum_{A=1}^{M}\frac{1}{2m_A}\nabla_A^2 - \sum_{i=1}^{N}\sum_{A>i}^{M}\frac{Z_A}{r_{iA}} + \sum_{i=1}^{N}\sum_{j>i}^{N}\frac{1}{r_{ij}} + \sum_{A=1}^{M}\sum_{B>A}^{M}\frac{Z_A Z_B}{R_{AB}} \right)\Psi_j && (2.3)\\
&= E_j\Psi_j \ . && (2.4)
\end{aligned}$$

Ψ_j denotes the time-independent wave function. The electronic structure Hamiltonian $\hat{H}$ can be separated (eq. 2.2) into kinetic energies $\hat{T}$ of electrons (e) and nuclei (n) and potential energy $\hat{V}$ of all possible *Coulomb* interactions between nuclei and electrons (en, ee, NN). In eq. 2.3 i and j are electron indices and A and B the indices for the nuclei with masses m_A and m_B and charges Z_A and Z_B. The variables r and R refer to particle distances. ∇^2 is the Laplacian of a particle. The eigenvalue of the equation is the energy E_j of the state.

Analytically solving the stationary *Schrödinger* equation is only possible for one particle or two-particle systems that can be described in terms of a reduced mass (e.g. H and He^+). To simplify the problem the *Born-Oppenheimer* approximation was introduced.[49] The nuclear

and electronic degrees of freedom are separated which is a reasonable approximation because the wave function describing the movement of electrons changes instantaneously upon a change in the external nuclear potential (i.e. nuclear movement). In the *Born-Oppenheimer* approximation the nuclei are considered to be static and only the electrons are described by a wave function $\Psi_{\mathrm{elec}}(\vec{\mathrm{r}};\vec{\mathrm{R}})$ which contains the electronic coordinates $\vec{\mathrm{r}}$ explicitly and parametrically depends on the position of the nuclei $\vec{\mathrm{R}}$. The corresponding electronic *Schrödinger* equation can be written as follows:

$$\begin{aligned} \hat{\mathrm{H}}_{\mathrm{elec}}\Psi_{\mathrm{elec,j}} &= (\hat{\mathrm{T}}_{\mathrm{e}} + \hat{\mathrm{V}}_{\mathrm{eN}} + \hat{\mathrm{V}}_{\mathrm{ee}})\Psi_{\mathrm{elec,j}} && (2.5)\\ &= \mathrm{E}_{\mathrm{elec,j}}\Psi_{\mathrm{elec,j}}\ . && (2.6) \end{aligned}$$

The aim of the *Hartree-Fock* formalism is to solve the electronic *Schrödinger* equation. Thereby the approximation which is used for the wave function Ψ ($= \Psi_{\mathrm{elec,j}}$) is a *Slater* determinant [50] (SD) of one particle functions $\chi_{\mathrm{i}}(\vec{\mathrm{x}})$ for each electron:

$$\Psi(\vec{\mathrm{x}}_1,\vec{\mathrm{x}}_2,...,\vec{\mathrm{x}}_{\mathrm{N}}) = \frac{1}{\sqrt{\mathrm{N!}}}\begin{vmatrix} \chi_1(\vec{\mathrm{x}}_1) & \chi_2(\vec{\mathrm{x}}_1) & \cdots & \chi_{\mathrm{N}}(\vec{\mathrm{x}}_1) \\ \chi_1(\vec{\mathrm{x}}_2) & \chi_2(\vec{\mathrm{x}}_2) & \cdots & \chi_{\mathrm{N}}(\vec{\mathrm{x}}_2) \\ \vdots & \vdots & \ddots & \vdots \\ \chi_1(\vec{\mathrm{x}}_{\mathrm{N}}) & \chi_2(\vec{\mathrm{x}}_{\mathrm{N}}) & \cdots & \chi_{\mathrm{N}}(\vec{\mathrm{x}}_{\mathrm{N}}) \end{vmatrix} = |\Psi\rangle\ . \qquad (2.7)$$

N denotes the number of electrons, the one particle functions are spin orbitals. They are the product of a spatial orbital ψ and a spin function $\delta(\mathrm{s})$ ($\delta = \alpha,\beta$). Consequently the coordinate $\vec{\mathrm{x}}_{\mathrm{i}}$ of the spin orbitals is a combined space-spin coordinate. The slater determinant obeys the *Pauli* principle. [51] For fermions it states that the wave function has to be antisymmetric upon the exchange of two electrons.

To find the best SD to describe a quantum system, the variational principle is applied. Thereby a trial wave function $\tilde{\Phi}(\mathrm{c_k})$ which depends on certain parameters is introduced. For a set of parameters $\{\mathrm{c_k}\}$, the energy of the trial wave function is minimized:

$$\frac{\partial}{\partial \mathrm{c_k}}\langle\tilde{\Phi}|\hat{\mathrm{H}}|\tilde{\Phi}\rangle = \frac{\partial}{\partial \mathrm{c_k}}\tilde{\mathrm{E}} = 0\ . \qquad (2.8)$$

The energy of this trial wave function is an upper limit to the exact ground state energy $\tilde{\mathrm{E}} \geq \mathrm{E_{exact}}$. In the following we will show that applying the *Roothaan-Hall* approach [52,53] enables calculation of the HF energy in a systematic fashion. Finding the best wave function for a quantum system thereby becomes a numerical minimization problem where expansion coefficients of the atomic basis orbitals are optimized.

Applying the variational principle to the stationary *Schrödinger* equation (2.2) using an SD ansatz for the wave function yields the *Fock* equation.[54] It is a time-independent eigenvalue (ε_a) equation using the spin orbitals $\chi_a(\vec{x}_i)$ as eigenfunctions:

$$\hat{f}(\vec{x}_i)\chi_a(\vec{x}_i) = \left[-\frac{1}{2}\nabla_i^2 - \sum_{A=1}^{M}\frac{Z_A}{r_{iA}} + \hat{v}^{HF}(\vec{x}_i)\right]\chi_a(\vec{x}_i) = \varepsilon_a\chi_a(\vec{x}_i)\ . \tag{2.9}$$

The *Fock* operator $\hat{f}(\vec{x}_i)$ is acting on electron i. The first and second terms of the operator correspond to the kinetic energy of electron i and its attractive *Coulomb* interactions with all M nuclei with charge Z_A. The variable r_{iA} denotes the distance of the electron i to a nucleus. The term $\hat{v}^{HF}(\vec{x}_i)$ is the *Hartree-Fock* potential which contains the average interaction of electron i with all other electrons and is defined as follows:

$$\hat{v}^{HF}(\vec{x}_i)\chi_a(\vec{x}_i) = \left(\sum_{b}^{N}\hat{J}_b(\vec{x}_i) - \hat{K}_b(\vec{x}_i)\right)\chi_a(\vec{x}_i)\ . \tag{2.10}$$

$\hat{J}_b$ is the *Coulomb* operator and $\hat{K}_b$ is the exchange operator. They are defined as follows:

$$\hat{J}_b(\vec{x}_i)\chi_a(\vec{x}_i) = \int\left(\chi_b^*(\vec{x}_j)\frac{1}{r_{ij}}\chi_b(\vec{x}_j)\right)d\vec{x}_j\chi_a(\vec{x}_i) \tag{2.11}$$

$$\hat{K}_b(\vec{x}_i)\chi_a(\vec{x}_i) = \int\left(\chi_b^*(\vec{x}_j)\frac{1}{r_{ij}}\chi_a(\vec{x}_j)\right)d\vec{x}_j\chi_b(\vec{x}_i)\ . \tag{2.12}$$

The *Coulomb* operator $\hat{J}_b(\vec{x}_i)$ operates on electron i in spin orbital χ_a, and its eigenvalue corresponds to the classical *Coulomb* repulsion with electron j in spin orbital χ_b. The exchange operator has no classical analogy, it is a consequence of the anti-symmetric many-body wave function. The exchange operator only acts on electrons i and j with parallel spin; for anti-parallel spin it vanishes. Unphysical self interaction, defined as the interaction of an electron with itself ($\chi_b = \chi_a$ in eq. 2.11 and 2.12), is avoided completely in HF, since the *Coulomb* and exchange integrals for self interactions cancel each other out ($\hat{J}_a(\vec{x}_i)\chi_a(\vec{x}_i) = \hat{K}_a(\vec{x}_i)\chi_a(\vec{x}_i)$). Summing the orbital energies and the expectation value of $\hat{v}^{HF}$ for each spin orbital the total *Hartree-Fock* energy is calculated:

$$E_{HF} = \sum_{a}^{N}\left(\varepsilon_a - \frac{1}{2}\langle\chi_a^*|\hat{v}^{HF}|\chi_a\rangle\right)\ . \tag{2.13}$$

In the *Roothaan-Hall* approach[52,53] the spatial part of the WF is expanded in a set of basis functions. They chose to use the atomic orbitals (AOs) related to analytically solving the

Schrödinger equation for the hydrogen atom. Then the ansatz for all spatial orbitals ψ_i is a linear combination of K atom-centered hydrogen-like atomic orbital functions $\varphi_\mu(\vec{r})$:

$$\psi_i = \sum_{\mu}^{K} C_{\mu i}\varphi_\mu(\vec{r}) \ . \tag{2.14}$$

Each spatial orbital has an expansion coefficient $C_{\mu i}$ which determines how much the AO contributes to the spatial orbital with index i. Those coefficients are the parameters that are varied during an optimization procedure. Inserting the expended ψ_i into the *Fock* equation (eq. 2.9) we end up with the following matrix eigenvalue equation:

$$\mathbf{FC} = \varepsilon\mathbf{SC} \ . \tag{2.15}$$

The K × K matrix **C** contains the AO coefficients. **F** denotes the Fock matrix for which the elements are defined as as:

$$\mathbf{F} = F_{\mu\nu} = \int \varphi_\mu^*(\vec{r_1})\hat{f}(\vec{r_1})\varphi_\nu(\vec{r_1})d\vec{r_1} \ . \tag{2.16}$$

The matrix **S** is the overlap matrix, its matrix elements are defined as:

$$\mathbf{S} = S_{\mu\nu} = \int \varphi_\mu^*(\vec{r_1})\varphi_\nu(\vec{r_1})d\vec{r_1} \ . \tag{2.17}$$

Finally, ε is a diagonal matrix containing the orbital eigenvalues.

The HF equations are iteratively solved within the self consistent field (SCF) approach shown above.[55] That is necessary because eq. 2.15 is non-linear as **F** depends on **C**. The calculation is started with an initial guess for the coefficient matrix $\mathbf{C}_0$. Next the *Roothaan-Hall* equation (eq. 2.15) is solved which gives rise to a new coefficient matrix $\mathbf{C}_1$. This matrix is again plugged into the *Roothaan-Hall* equation. This process is repeated until the difference in the total energy between $\mathbf{C}_{n-1}$ and $\mathbf{C}_n$ is below a user defined threshold, the convergence criterion.

2.1.2 Density functional theory (DFT)

The basic concept of DFT is to determine the energy of a system from its electron density. In particular the total energy of a system is a function of the electron density, which is a function itself of $\vec{r}$, the spatial coordinates. This was shown first by *Kohn* and *Hohenberg*.[56] This is a fundamental difference to other wave function based methods such as the *Hartree-Fock* method in which the *Schrödinger* equation has to be solved to obtain the energy of the system. The latter involves the computation of wave functions which depend on 3N spatial coordinates and N spin coordinates for an N electron system system. On the other hand the density used

in DFT only depends on one spatial coordinate and can be computed with less effort. DFT methods present the most cost effective approach for many applications.

The basis for DFT methods is provided by the two *Hohenberg-Kohn* theorems.[56] The first one is the existence theorem. It states that the density associated with a non-degenerated ground state wave function uniquely determines the potential and consequently all properties of the system.[55] The second theorem states that the true ground state electron density ρ_{exact} yields the lowest possible energy E_0. The energy $\tilde{E}$ associated with a suitable candidate density $\tilde{\rho}$ for a given system is always larger or equal E_0:

$$\tilde{E}(\tilde{\rho}) \geq E_0(\rho_{\mathrm{exact}}) \ . \tag{2.18}$$

The underlying idea of the *Kohn-Sham* method[57] is to construct a fictitious system of non-interacting electrons that have for their overall ground-state density the same density as the real system of interest where electrons do interact. The total energy of the system $E[\rho(\vec{r})]$ can be separated into the following parts:

$$E[\rho(\vec{r})] = T_{\mathrm{ni}}[\rho(\vec{r})] + V_{\mathrm{ne}}[\rho(\vec{r})] + V_{\mathrm{ee},\mathit{Coulomb}}[\rho(\vec{r})] + E_{\mathrm{XC}}[\rho(\vec{r})] \ . \tag{2.19}$$

$T_{\mathrm{ni}}[\rho(\vec{r})]$ represents the kinetic energy of the non-interacting system, $V_{\mathrm{ne}}[\rho(\vec{r})]$ represents the *Coulomb* interaction between nuclei electrons and $V_{\mathrm{ee},\mathit{Coulomb}}[\rho(\vec{r})]$ represents the classical electron repulsion. The term $E_{\mathrm{XC}}[\rho(\vec{r})]$ accounts for all energy contributions from phenomena neglected by the simplified approach. This includes the non-classical electron interaction and additionally a kinetic energy correction because the kinetic energy of the real system is not accounted correctly. Determining E_{XC} is challenging as an analytical solution is impossible for the general case of an inhomogeneous electron gas. Furthermore the E_{XC}-functionals can not be improved systematically. In practice a wide range of E_{XC}-functionals is available some of which will be presented in the end of this section.

Slater determinant wave functions are exact eigenfunctions for non-interacting systems. The electron density resulting from N electrons can be expressed as the sum of the single electron densities:

$$\rho = \sum_{i=1}^{N} |\psi_i|^2 \tag{2.20}$$

ψ_i represents an orbital for an electron i. Orbitals that minimize Eq. (2.19) satisfy the following eigenvalue equations

$$\hat{h}_i^{\mathrm{KS}} \psi_i = \varepsilon_i \psi_i \tag{2.21}$$

where the *Kohn-Sham* (KS) one-electron operator $\hat{h}_i^{KS}$ is defined as

$$\hat{h}_i^{KS} = -\frac{1}{2}\nabla_i^2 - \sum_{A=1}^{M} \frac{Z_k}{|\vec{r}_i - \vec{r}_k|} + \int \frac{\rho(\vec{r}')}{|\vec{r}_i - \vec{r}'|} d\vec{r}' + V_{XC} \tag{2.22}$$

and

$$V_{XC} = \frac{\delta E_{XC}}{\delta \rho} \ . \tag{2.23}$$

∇_i^2 represents the *Laplace* operator for an electron i at the position $\vec{r}_i$, Z_k represents the nuclei charge of a nucleus k at the position $\vec{r}_k$ and V_{XC} represents a functional derivative. To determine the *Kohn-Sham* orbitals they are expressed within a set of basis functions $\{\mu\}$. To calculate the individual orbital coefficients a secular equation with the matrix elements

$$F_{\alpha\beta} = \left\langle \mu_\alpha \middle| h_i^{KS} \middle| \mu_\beta \right\rangle \tag{2.24}$$

is solved. Obtaining the energy for a given structure is an iterative process within DFT calculations. As for the *Hartree-Fock* method a self-consistent field approach is used, but instead of the wave function the density (matrix) is guessed and subsequently updated until convergence (fig. 2.1). Please note that the sum of the eigenvalues cannot be simply related with the total energy because the KS system is non-interacting. The neglected interactions have to be included in the final energy using the exchange integral and the XC energy and potential (highlighted in red in fig. 2.1).

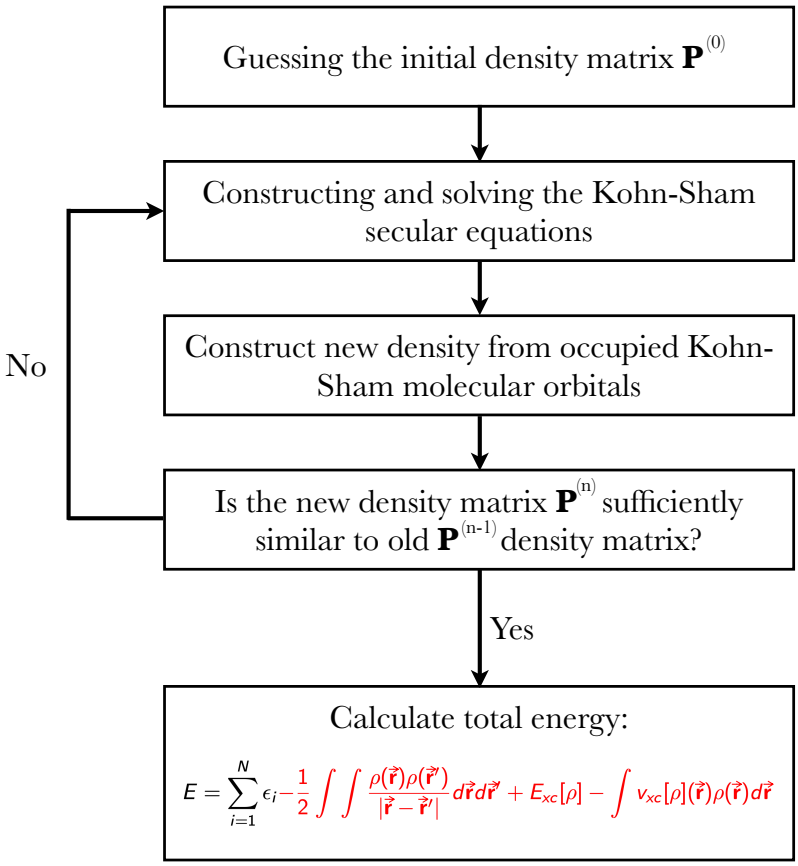

Figure 2.1: SCF algorithm used in DFT calculations.

The quality of the DFT simulations largely depends on the XC functional. It is separated into the correlation and exchange parts which are developed separately:

$$\mathrm{E_{XC}}[\rho] = \mathrm{E_X}[\rho] + \mathrm{E_C}[\rho] \ . \tag{2.25}$$

Among the first approximations to the XC functional was the local density (LDA) approach. Thereby the exchange-correlation functional of the inhomogeneous electron gas is replaced by the exchange-correlation functional of the homogeneous electron gas:

$$\mathrm{E_{XC}^{LDA}}[\rho] = \int \rho(\vec{\mathrm{r}}) \varepsilon^{\mathrm{XC}}[\rho(\vec{\mathrm{r}})] \mathrm{d}\vec{\mathrm{r}} \ . \tag{2.26}$$

For the homogeneous electron gas the exchange part can be solved analytically while the correlation part is only solvable for high- and low-density limits.[58] The model of the homogeneous electron gas considers a homogeneous positive background charge, while in molecular systems the positive charges are localized at the nuclei. Consequently the error in the LDA functional is quite large. The model can be improved by accounting for the inhomogeneity of the electron gas by also including the gradient of the electron density in the XC functional:

$$E_{XC}^{GGA}[\rho] = \int \varepsilon^{XC}[\rho, \nabla\rho]d\vec{r} \,. \tag{2.27}$$

Functionals of this class are called generalized gradient approximation (GGA) functionals. For ε^{XC} there is no analytical solution. Consequently the number of GGA functionals with different approaches is relatively large both for the exchange [46,59,60] and correlation [46,60,61,62] part. In the different implementations various functional forms how the gradient is introduced are common. The Perdew-Burke-Ernzerhof exchange and correlation functionals used together give rise to the PBE functional [46] which is a popular choice for periodic systems such as the semiconductors simulated in this work or metals.

Experience indicates that GGA functionals have certain systematic errors. For instance, they tend to underestimate barrier heights of chemical reactions. *Hartree-Fock* theory, on the other hand, tends to overestimate barrier heights. [55] Similarly band gaps tend to be underestimated by GGA functionals and overestimated by HF. In an effort to tune DFT functionals towards experimental chemical results the class of hybrid functionals was created. For those functionals the exact *Hartree-Fock* exchange (calculated for *Kohn-Sham* orbitals) is mixed with a certain weight α with the exchange of a GGA or the LDA functional:

$$E_X^{hybrid} = \alpha E_X^{exact} + (1-\alpha)E_X^{DFT} \,. \tag{2.28}$$

The coefficient α is found by fitting to experimental data, for the functional PBE0 it is 25 %. [63] Same as the HF method any KS DFT formally scales with N^4 (N: number of atoms) due to the four center integration (eq. 2.11). Still the computational demand of hybrid DFT is larger than for LDA and GGA DFT. The reason is that the calculation of exact exchange demands an extra step throughout the SCF procedure to calculate the non-local exchange integrals (see eq. 2.12). [55] In periodic calculations hybrid DFT is even more expensive than LDA and GGA DFT because the exchange acts non-locally. That has a big impact on computational demand in an infinitely extended (idalized) periodic solid state system whereas the impact for a molecular system is limited. To reduce the scaling for solids range-separated hybrid functionals have been introduced. Thereby the exact exchange part is screened to only act short ranging (SR). The long ranging (LR) interaction is described using a LDA or GGA DFT method. In this work we used the Heyd, Scuseria and Ernzerhof (HSE) functional with the following XC functional: [47]

$$E_{XC}^{HSE0x} = \frac{3}{4}E_X^{PBE,SR}(\omega) + \frac{1}{4}E_X^{exact,SR}(\omega) + E_X^{PBE,LR}(\omega) + E_C^{PBE} \,. \tag{2.29}$$

ω denotes the HF screening parameter, which is set to 0.3 $Å^{-1}$ for HSE03 and to 0.2 $Å^{-1}$ for HSE06. [47] For ω=0 the functional reduces to the PBE0 functional. We use HSE06 to calculate

accurate band gaps, as PBE is known to underestimated band gaps by up to 100 % in extreme cases.[64]

2.2 Periodic systems

The kesterite absorber in a thin-film solar cell is a crystal which contains a number of atoms in the order of the *Avogadro* constant ($6.02 \times 10^{23} \frac{1}{\text{mol}}$). To explicitly simulate all of them quantum-chemically is impossible due to the required computational demand. To enable computation the crystal symmetry of an ideal crystal is exploited. Real crystals exhibit defects and grain boundaries and are finite. Still their properties can be estimated by considering an idealized crystal which extends infinitely in all directions. The idealized crystal is fully characterized by a small structure which contains (at least) all symmetry-inequivalent atoms called unit cell. The smallest possible unit cell which contains all information about the periodic system is called *Wigner-Seitz* cell. The lattice of the unit cell is characterized by the three basis vectors $\vec{a}_1$, $\vec{a}_2$, $\vec{a}_3$ in real space. This structure is infinitely repeated through translational symmetry along the basis vectors of the unit cell. So every real space lattice position $\vec{R}$ in the crystal can be described as a linear combination of the three unit cell basis vectors:[65]

$$\vec{R} = n_1\vec{a}_1 + n_2\vec{a}_2 + n_3\vec{a}_3 \ , \tag{2.30}$$

n_i are the integer weights of the different basis vectors in real space. Reciprocal space is the space in which the *Fourier* transform of a real space function (e.g. spatial wave function) is represented. It is often useful to describe properties like the electron density of a periodic crystal. A reciprocal lattice can be constructed, thereby the real space lattice vector $\vec{R}$ gets transformed to the reciprocal space lattice vector $\vec{K}$:

$$\vec{K} = m_1\vec{b}_1 + m_2\vec{b}_2 + m_3\vec{b}_3 \ , \tag{2.31}$$

where m_i are the integer weights of the reciprocal lattice vectors $\vec{b}_i$. The reciprocal lattice vectors are defined as follows:[65]

$$\vec{b}_1 = 2\pi \cdot \frac{\vec{a}_2 \times \vec{a}_3}{\vec{a}_1 \cdot (\vec{a}_2 \times \vec{a}_3)} \tag{2.32}$$

$$\vec{b}_2 = 2\pi \cdot \frac{\vec{a}_3 \times \vec{a}_1}{\vec{a}_1 \cdot (\vec{a}_2 \times \vec{a}_3)} \tag{2.33}$$

$$\vec{b}_3 = 2\pi \cdot \frac{\vec{a}_1 \times \vec{a}_2}{\vec{a}_1 \cdot (\vec{a}_2 \times \vec{a}_3)} \ . \tag{2.34}$$

The absolute of each reciprocal lattice vector is the reciprocal of the corresponding real space vector times 2π (stems from *Fourier* transform): $|\vec{b}_i| = 2\pi \times |\vec{a}_i|^{-1}$. A crystal orbital (a one electron wave function defined by an SD) which describes a periodic potential, like in the unit cell of the ideal crystal has to fulfill *Bloch*'s theorem:[66]

$$\psi(\vec{r} + \vec{R}, \vec{k}) = e^{i\vec{k}\cdot\vec{R}}\psi(\vec{r}, \vec{k}) \ , \tag{2.35}$$

which states that the wave function obeys the same translational symmetry as the unit cell. The vector $\vec{k}$ corresponds to the crystal momentum in periodic systems. It is the solid state equivalent to the wave vector $\vec{k}$ for free particle matter waves according to *de Broglie*.[67] The vector $\vec{k}$ is proportional to the momentum of the particle (wave):

$$\vec{p} = \frac{h}{2\pi}\vec{k} = \hbar\vec{k} \ , \tag{2.36}$$

where h ($\hbar$) is the (reduced) Planck constant. Functions which fulfill *Bloch*'s theorem are called *Bloch* orbitals. They can be expressed in terms of $\vec{r}$ (real space) or $\vec{k}$ (reciprocal or momentum space). The equivalent to the *Wigner-Seitz* cell in k-space is called the first Brillouin zone (BZ), it represents the smallest possible unit cell in k-space. The BZ for kesterite Cu_2ZnSnS_4 is shown in fig. 2.2 as an example.

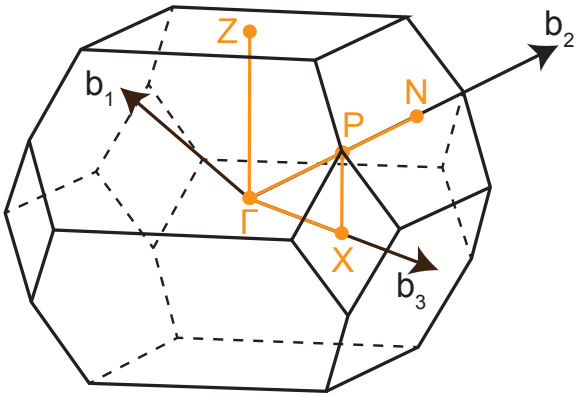

Figure 2.2: *Brillouin* zone of the space group $I\bar{4}$ for the Cu_2ZnSnS_4 kesterite unit cell with special high symmetry points highlighted in orange.

To carry out HF (or DFT) calculations for the idealized crystal the wave function (or electron density) of one electron $\psi_i(\vec{k}, \vec{r})$ (in solids also called one band) is expressed as a linear combination of K *Bloch* orbitals Φ_μ $(\vec{k},\vec{r})$ (or their electron density):

$$\psi_i(\vec{k}, \vec{r}) = \sum_{\mu}^{K} C_{\mu i}(\vec{k})\Phi_\mu(\vec{k}, \vec{r}) \ . \tag{2.37}$$

With this ansatz the HF or DFT matrix equations are solved with the SCF approach to obtain the optimal coefficients $C_{\mu i}(\vec{k})$:

$$\mathbf{F}(\vec{k})\mathbf{C}(\vec{k}) = \varepsilon(\vec{k})\mathbf{S}(\vec{k})\mathbf{C}(\vec{k}) \ . \tag{2.38}$$

The band eigenvalues depend on $\vec{k}$ which means that the HF or DFT calculations have to be carried out at various k-points throughout the first BZ. To determine properties which do not depend on the curvature of $E(\vec{k})$ along certain directions like structure relaxations, total energy or density of states the Monkhorst-Pack scheme is used.[68] Thereby the first BZ is sampled with equally spaced grid points along every reciprocal basis vector. The number of grid points is increased until the property of interest converges. If the property of interest depends on $\vec{k}$ like the band energy $\varepsilon(\vec{k})$, the $\vec{k}$ points are sampled along lines between high symmetry points (e.g. Z-Γ-X-P-Γ-N in fig. 2.2) in the first BZ.

2.2.1 Band structures and density of states (DOS)

Each single electron wave function represents a different molecular orbital extending through the whole solid. In molecular orbital (MO) theory the number of MOs equals the number of involved atomic orbitals (AOs). In a molecular bond between two hydrogen atoms for example we obtain two MOs, one binding and one anti-binding with a certain energy gap in between. In an N atom long chain of H atoms (so a 1-dimensional solid) there are 2N MOs. For large N (like the number of atoms in a real solid) the number of energy levels increases to a point that the difference in energy between them becomes negligible and the states form a quasi continuous energy band. Hence the name band structure was chosen for a plot of $\varepsilon(\vec{k})$. Exemplary the band structure of CZTS is plotted on the left in fig. 2.5.

All band energies $\varepsilon(\vec{k})$ are plotted over $\vec{k}$ along certain high symmetry path in BZ to obtain the band structure of a solid. Bands up to the so called *Fermi* energy E_F are filled at 0K.

Filled bands below E_F which arise from the valence electrons are referred to as valence bands (VB). Bands above E_F are called conduction band (CB). The gap in between them is called band gap E_g. There are three different classes of solids which are labeled according their conductivity: metallic conductor, semi-conductor and insulator (fig. 2.3). No band gap enables conductivity because additional electrons can be transmitted through the unoccupied states in the conductions band. If the band gap gets large, the CB becomes completely unavailable resulting in insulating behavior.

The band gap itself can be direct or indirect (fig. 2.4). A direct band gap means that the maximum of the VB is at the same $\vec{k}$ vector as the minimum of the CB. To excite an electron only a photon with more than the band gap energy is needed. An indirect band gap means that the maximum of the VB is not at the same $\vec{k}$ vector as the minimum of the CB, thus

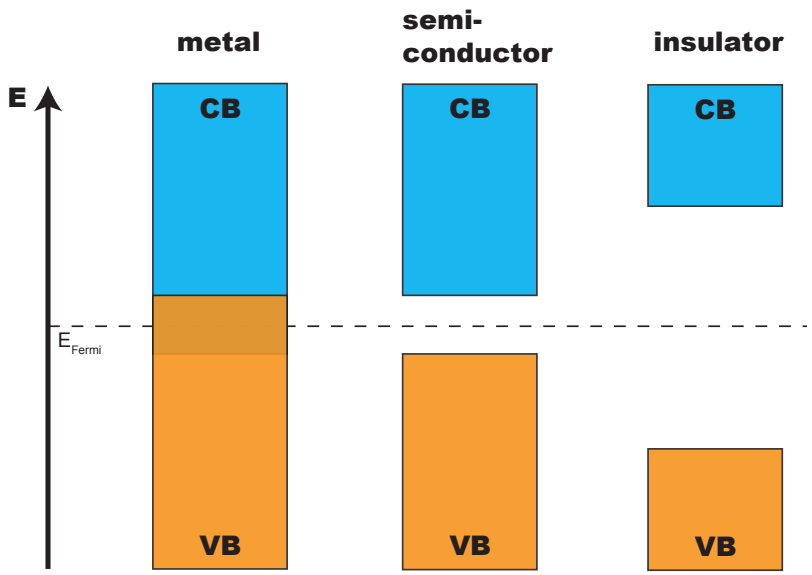

Figure 2.3: Schematic illustration of the band structures of metals, semi-conductors and solids. VB: valence band, CB: conduction band.

additional momentum transfer is needed to excite an electron. Solar cells and also many other opto-electrical devices are supposed to work using visible light, which carries nearly no momentum due to a relatively high wavelength. Thus direct band gap materials are used in opto-electrical devices.

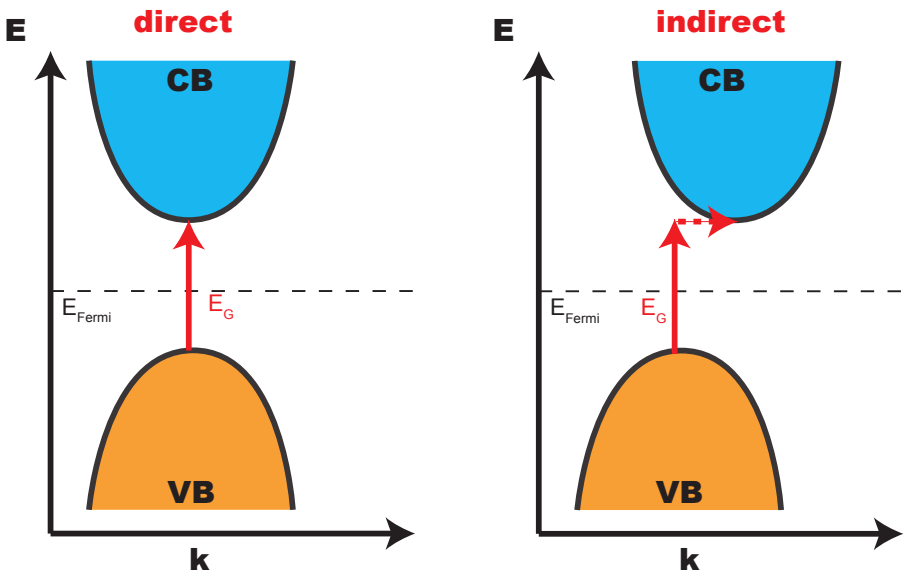

Figure 2.4: Schematic illustration of a direct and indirect band gap E_g. VB: valence band, CB: conduction band.

The computation of the band structure can be demanding because a number of scans in the BZ are necessary. Often the required information about the electronic structure (e.g. the band gap) can be extracted from the so called density of states plot, which can be computed by grid sampling of the BZ. The density of states is the number of different states at a particular energy level which electrons can occupy. It is defined as follows: [65]

$$D_i(E) = \frac{1}{V_{BZ}} \int_{BZ} d\vec{k}\delta(E - E_i(\vec{k})) \ . \tag{2.39}$$

$D_i(E)$ denotes the density of states at a certain energy E of the ith band, V_{BZ} refers to the BZ volume, over which is integrated. The DOS is closely related to the band structure, as can be seen in fig. 2.5 at the example of CTZS. The higher the density of bands in a certain energy interval in the band structure the larger the peak of the total DOS. The DOS plot also features projected DOS for each element, which shows the contribution to the total DOS for each element separately.

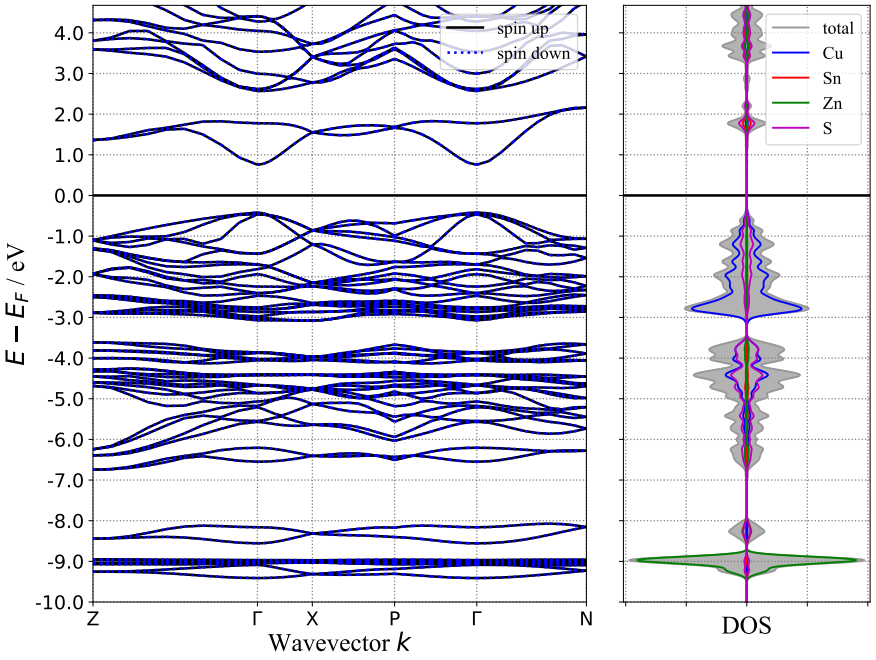

Figure 2.5: HSE06 Band structure and DOS for the Cu_2ZnSnS_4 kesterite structure.

2.2.2 Basis sets and pseudopotentials

The wave function or its density is expanded in basis sets for HF and DFT respectively. For molecular systems atom centered basis sets are used, more specifically mostly *Gaussian* type

orbital (GTO) basis sets.[55,69] They often provide more orbitals for the valence electrons than for the core electrons (split valence) as opposed to the minimal amount (minimal basis set). Naturally they perform well when describing localized electrons but they are not very efficient when it comes to describing delocalized systems like the electron gas of a metal. If GTOs are used in solid state calculations they suffer from numerical instabilities due to linearly dependent basis functions at different atoms because the basis set is non-orthogonal.[70]

To simulate solids another type of basis functions is commonly used: plane wave (PW) basis sets.[71] PW basis sets are not atom centered. Also PW basis function are orthogonal which has computational advantages. In this work we exclusively used PW basis sets. Consequently they will be discussed in more detail here. *Bloch*'s theorem (eq. 2.35) formulates a condition that all solutions $\psi_n(\vec{k},\vec{r})$ of the *Schrödinger* equation (eq. 2.4) for a periodic potential (e.g. determined by the crystal lattice) have to meet:

$$\psi_n(\vec{k},\vec{r}) = e^{i\vec{k}\cdot\vec{r}} \cdot u_n(\vec{r}) \ . \tag{2.40}$$

The index n refers to the n-th band, $\vec{k}$ refers to any allowed wave vector for the electron and $u_n(\vec{r})$ refers to a function with the periodicity of the lattice. The cell periodic function $u_n(\vec{r})$ can be expressed by expanding it to a finite number of L plane waves whose wave vectors $\vec{K}$ are reciprocal lattice vectors of the crystal:

$$u_n(\vec{r}) = \sum_{\vec{K}}^{L} C_{n\vec{K}} e^{i\vec{K}\cdot\vec{r}} \ . \tag{2.41}$$

$C_{n\vec{K}}$ denotes the expansion coefficient of each basis function. By combining the two equations above we arrive at the final formulation of the crystal wavefunction for the n-th band:

$$\psi_n(\vec{k},\vec{r}) = \sum_{\vec{K}}^{L} C_{n\vec{K}} e^{i(\vec{k}+\vec{K})\cdot\vec{r}} \ . \tag{2.42}$$

As the elements of $\vec{K}$ are reciprocal lattice vectors scaled by integers we obtain plane waves with nodes at the cell boundaries. The number of plane waves L depends on the energy-cutoff E_{cut} which is defined as follows:

$$E_{cut} = \frac{1}{2}\vec{K}_{max} \ . \tag{2.43}$$

A higher cutoff includes plane waves with more nodes which leads to a more accurate description of the electron density. PWs can more efficiently describe delocalized electrons than localized electrons.

In the core region the electrons are highly localized while the valence electrons are more delocalized in comparison. Describing core electrons with a PW basis set is more expensive than describing the valence electrons. If the research question is independent from the core electrons like in this thesis, only the valence electrons are explicitly described with the PW basis set. The core electrons are replaced with a so called pseudo potential. It contains the summarized potential of all core electrons in analytical form and enables much smaller energy cutoffs in comparison to all electron calculations. One of the most popular choices for pseudo potentials in plane wave calculations is the projector augmented-wave (PAW) method [72,73] which was also used in this work. The all electron wave function is portioned into an inner part up to the radius r_{aug} and an outer region beyond that. The outer part is explicitly described with the PW basis. The inner part of the core WF is simplified, it is expanded in a radial function and spherical harmonics functions. [72] While other pseudo potentials modify the Hamiltonian with an additional potential, the PAW method does not. It rather smoothes out the inner part of the core electron orbitals.

2.3 *Birch-Murnaghan* (B-M) Equation of state

In this thesis we study the behavior of the kesterite absorber materials at elevated pressures. We essentially compare enthalpies ($H(\mathrm{P}) = \mathrm{E} + \mathrm{PV}$) of different structural models in a certain pressure range. To calculate the enthalpy and also the pressure itself we carry out a volume scan (fig. 2.6 shows example for kesterite CZTS). In a volume scan a structural model is optimized at different unit cell volumes which are forced to be constant. The scan is typically carried out around the equilibrium volume.

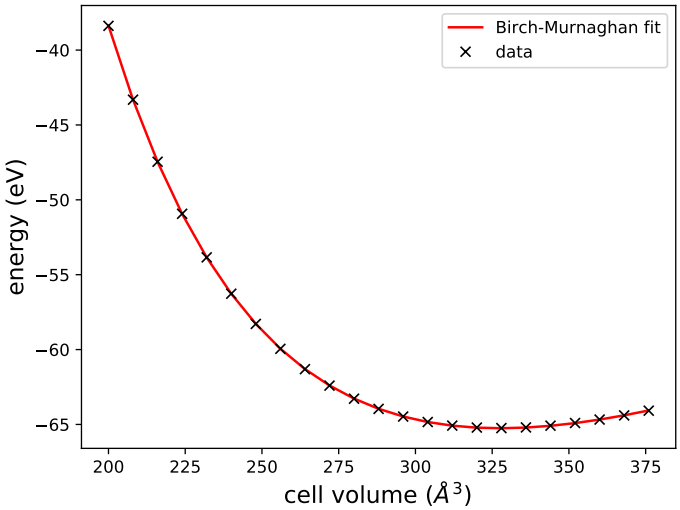

Figure 2.6: Volume scan and fitted B-M equation of state for the Cu_2ZnSnS_4 kesterite structure.

We fit the volume scan data to the *Birch-Murnaghan* isothermal equation of state. The B-M equation of state is a relationship between the volume of a body and the pressure to which it is subjected. Third-order Birch-Murnaghan isothermal equation of state is defined as follows:[74]

$$E(V) = E_0 + \frac{9\,V_0 B_0}{16}\left\{\left[\left(\frac{V_0}{V}\right)^{\frac{2}{3}} - 1\right]^3 B_0^{'} + \left[\left(\frac{V_0}{V}\right)^{\frac{2}{3}} - 1\right]^2 \left[6 - 4\left(\frac{V_0}{V}\right)^{\frac{2}{3}}\right]\right\} . \tag{2.44}$$

E_0 denotes the energy per unit cell at zero pressure, B_0 the bulk modulus at zero pressure, V_0 the reference volume at zero pressure; $B_0^{'}$, pressure derivative of the bulk modulus at zero pressure. We calculate the slope of the equation of state which is related to the pressure:

$$P(V) = -\left(\frac{\partial \mathrm{E}}{\partial \mathrm{V}}\right) \tag{2.45}$$

$$P(V) = \frac{3B_0}{2}\left[\left(\frac{V_0}{V}\right)^{\frac{7}{3}} - \left(\frac{V_0}{V}\right)^{\frac{5}{3}}\right]\left\{1 + \frac{3}{4}(B_0^{'} - 4)\left[\left(\frac{V_0}{V}\right)^{\frac{2}{3}} - 1\right]\right\} . \tag{2.46}$$

With the pressure we can finally calculate the enthalpy $H(\mathrm{P})$ to compare between different structural models.

3 Publications

3.1 Paper A

"Pressure-induced structural and electronic transitions in kesterite-type Cu_2ZnSnS_4"

Efthimiopoulos, I., Küllmey, T., Speziale, S., Pakhomova, A. S., Quennet, M., Paulus, B., Ritscher, A., Lerch, M. and Koch-Müller, M., *J. Appl. Phys.* **2018**, *124*(8), 085905

DOI: 10.1063/1.5047842

URL: `http://www.doi.org/10.1063/1.5047842`

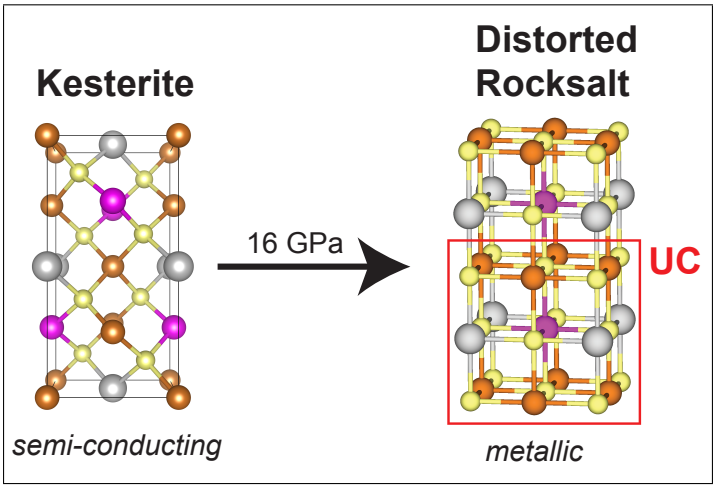

Graphical abstract of Paper A.

Contributions: The concept for this paper was developed by I.E., B.P. and M.L. The samples where prepared by A.R. The high-pressure XRD experiments where carried out by I.E. and S.S. with support of A.P. T.K. and M.Q. carried out the DFT calculations. M.Q. carried out test calculations to find suitable DFT settings for this project. T.K. carried out the equilibrium and high-pressure calculations and the subsequent data analysis. The initial draft of the paper was written by I.E. and T.K. Editing was also carried out by I.E. and T.K. with input from all other authors. The whole project was supervised by B.P., M.L. and M.K.-M.

3.2 Paper B

"High-pressure behavior of disordered kesterite-type Cu_2ZnSnS_4"

Efthimiopoulos, I., Küllmey, T., Speziale, S., Pakhomova, A. S., Quennet, M., Paulus, B., Ritscher and A., Lerch, M., *Appl. Phys. A* **2021**, *127*, 616

DOI: 10.1007/s00339-021-04745-w

URL: `http://www.doi.org/10.1007/s00339-021-04745-w`

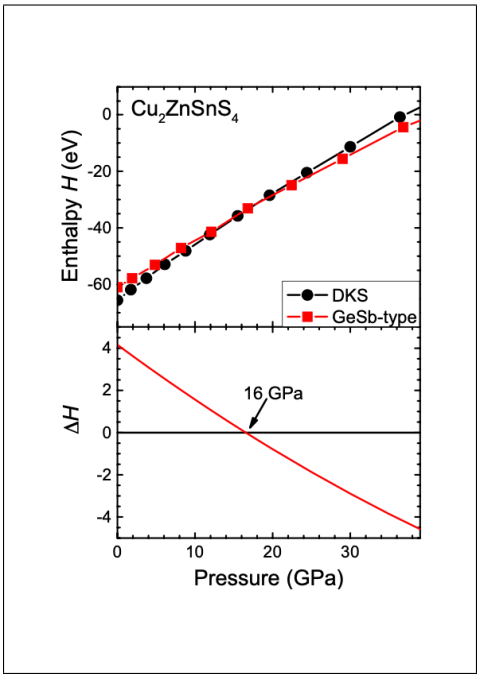

Graphical abstract of Paper B.

Contributions: The concept for this paper was developed by I.E., B.P. and M.L. The samples where prepared by A.R. The high-pressure XRD experiments where carried out by I.E. and S.S. with support of A.P. T.K. and M.Q. carried out the DFT calculations. M.Q. carried out test calculations to find suitable DFT settings for this project. T.K. carried out the equilibrium and high-pressure calculations and the subsequent data analysis. The initial draft of the paper was written by I.E. and T.K. Editing was carried out by I.E. with input from all other authors. The whole project was supervised by B.P. and M.L.

3.3 Paper C

"Calculation for high-pressure behaviour of potential solar cell materials Cu_2FeSnS_4 and Cu_2MnSnS_4"

Küllmey, T., González, M., Heppke, E. M. and Paulus, B., *Crystals* **2021**, *11*(2), 1–19

DOI: 10.3390/cryst11020151

URL: `http://www.doi.org/10.3390/cryst11020151`

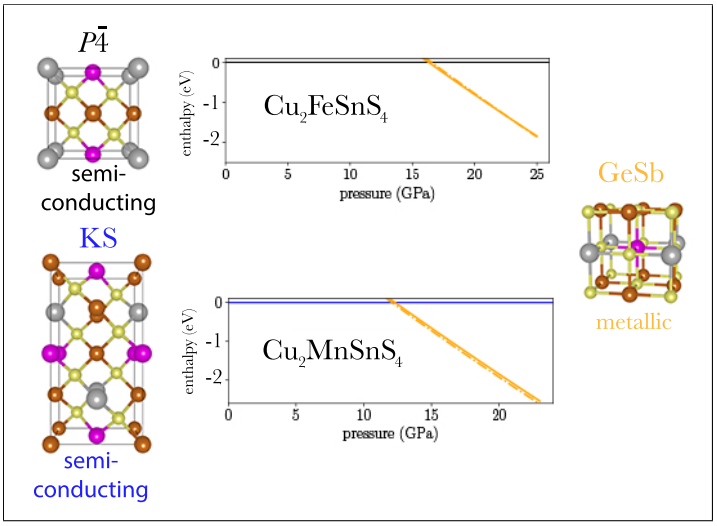

Graphical abstract of Paper C. ©2021 MDPI

Contributions: The concept for this paper was developed by T.K., B.P. and E.H. The DFT calculations were set up and tested by T.K. M.G. carried out high-pressure DFT calculations under close supervision of T.K. The data analysis was done by T.K. The initial draft of the paper was written by T.K. Editing was carried out by T.K. with input from all other authors. The whole project was supervised by B.P.

3.4 Paper D

"high-pressure behavior and disorder for Ag_2ZnSnS_4 and Ag_2CdSnS_4"

Küllmey, T., Hein, J., Heppke, E. M., Efthymiopoulos, I. and Paulus, B., manuscript will be submitted to *ACS Omega* with minor changes

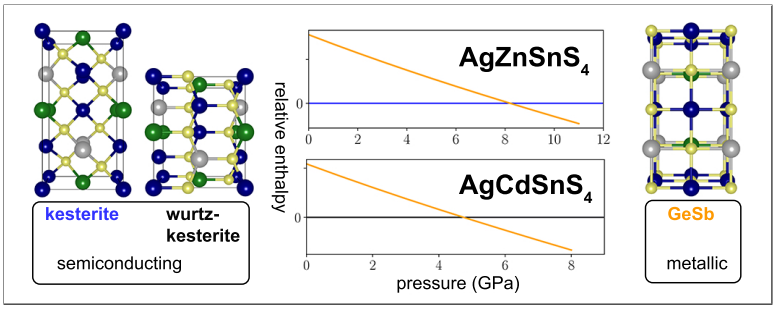

Graphical abstract of Paper D.

Contributions: The concept for this paper was developed by T.K., B.P. and E.H. The DFT calculations were set up and tested by T.K. J.H. carried out high-pressure DFT calculations under close supervision of T.K. The data analysis was done by T.K. The initial draft of the paper was written by T.K. Editing was carried out by T.K. with input from all other authors. The whole project was supervised by B.P.

High pressure behavior and disorder for Ag_2ZnSnS_4 and Ag_2CdSnS_4

Tim Küllmey,[*,†] Jakob Hein,[†] Eva M. Heppke,[‡] Ilias Efthymiopoulos,[¶,§] and Beate Paulus[†]

†*Institut für Chemie und Biochemie, Freie Universität Berlin, Arnimallee 22, 14195 Berlin, Germany*

‡*Institut für Chemie, Technische Universität Berlin, Strasse des 17. Juni 135, 10623 Berlin, Germany*

¶*Section 3.6: Chemistry and Physics of Earth Materials, Deutsches GeoForschungsZentrum (GFZ), Telegrafenberg, 14473 Potsdam, Germany*

§*Institute of Physics, University of Greifswald, Felix-Hausdorff-Strae 6, 17489 Greifswald, Germany*

E-mail: tim.kuellmey@fu-berlin.de

Abstract

We have carried out first principle calculations to simulate Ag_2ZnSnS_4 and Ag_2CdSnS_4. We calculated enthalpies of different plausible structural models (kesterite-type, stannite-type, wurtzkesterite-type, wurtzstannite-type and GeSb-type) to identify low and high pressure phases. For Ag_2ZnSnS_4 we predict the following transition: kesterite-type $\xrightarrow{8.2\text{GPa}}$ GeSb-type. At the transition pressure the electronic structure changes from semi-conducting to metallic. For Ag_2CdSnS_4 we cannot decide which of the experimentally observed structures (kesterite-type or wurtzkesterite-type) is the ground state structure, because their energy difference is too small. At 4.7 GPa however we predict a transition to GeSb-type structure with metallic character for both structures.

Preliminary manuscript for ACS omega

Regarding the sensitivity of the material to disorder, a major drawback for solar-cell applications, Ag_2CdSnS_4 behaves similarly to Cu_2ZnSnS_4, both show a high tendency to cationic disorder. In contrast, the disordered structures in Ag_2ZnSnS_4 are much higher in energy and therefore the material is less affected by disorder.

Keywords

DFT, materials, AZTS, solar cell absorber, kesterite, high pressure

Introduction

In the research to improve solar energy conversion, one of the well explored materials for thin-film solar-cell absorbers is the direct-band gap semiconductor Cu_2ZnSnS_4 (CZTS) and the corresponding selenide $Cu_2ZnSnSe_4$ (CZTSe).[1–3] The elements which make up those materials are naturally abundant and relatively environmentally friendly. Up to this point they have shown conversion efficiencies up to 12.5%.[4,5]

On the one side, compressive stress is of importance for the use as thin film solar cells as they can be sputtered. The ion bombardment in the sputtering deposition leads to compressive stress.[6,7] In CZTS(e) solar cells either the absorber material itself is sputtered[1] or the buffer layer CdS, the transparent conducting oxide ZnO and the antireflection coating MgF_2 layer on top are sputtered.[5] In a previous experimental and theoretical study on kesterite-type Cu_2ZnSnS_4 (fig. 1 a) we have investigated the high pressure behavior to probe its reaction to compressive stress.[8] In this study our DFT calculation matched the experimental high pressure results very well, correctly predicting an irreversible phase transition towards a metallic GeSb-type structure (fig. 1 b) at 16 GPa.

In this study we will compare the two materials Ag_2ZnSnS_4 (AZTS) and Ag_2CdSnS_4 to Cu_2ZnSnS_4 with regards to their high pressure behavior. Ag_2ZnSnS_4 has already been tested as solar cell absorber, but is shows limited efficiencies under 1 % if used in a pn-

(a) KS (b) GeSb

Figure 1: Structural models for (a) kesterite-type (KS, $I\bar{4}$) and (b) GeSb-type ($P4/mmm$) Cu_2ZnSnS_4. Copper: Cu, pink: Zn, grey: Sn and yellow: S. For the GeSb-type structure we show two unit cells (stacked along c-axis)

homojunction.[9] The efficiency can be increased to 4.5 % if the material is combined in a CZTS/AZTS heterojunction.[10] Theoretical work proposes a CdS/ACZTS/CZTS (n/p/p+) solar cell with a potential efficiency close to 20 %.[11] Doping $Cu_2ZnSnSe_4$ with 10 % Ag leads to cells with up to 10.2 % efficiency[12] revitalizing the interest in AZTS and AZTSe.[3]

Ag_2CdSnS_4 is not a suitable candidate for solar cell absorbers as it contains Cd which is toxic and avoiding its use is one of the advantages of CZTS technology over better performing CdTe thin film solar cells. Using it in small amounts may be tolerable, doping Cu_2ZnSnS_4 with 25 % Cd and 5 % Ag led to cells with 10.8 % efficiency.[12] Nevertheless we include Ag_2CdSnS_4 in our study to understand the influence of the bivalent cation on the high pressure behavior.

On the other side, one of the biggest issues with Cu_2ZnSnS_4 is Cu-Zn cationic disorder.[13,14] The main reason why Cu (ionic radius: 0.77 Å[15]) and Zn (ionic radius: 0.74 Å[15]) can be interchanged easily is their similar ionic radius. In the Ag (ionic radius: 1.15 Å[15]) analogue Ag_2ZnSnS_4 cationic disorder is expected to be less present due to the bigger difference in size of Ag to Zn in comparison to Cu.[16] We also include Ag_2CdSnS_4 to verify how the stability of disordered structures changes if the bivalent ion gets larger (ionic radius Cd: 0.95 Å[15]), getting closer toward the ratio present in Cu_2ZnSnS_4.

Therefore we will apply first principle DFT methods to investigate both, the pressure dependence of Ag_2ZnSnS_4 and Ag_2CdSnS_4 and the tendencies of the materials to cationic disorder.

Computational details

Calculation set-up

The periodic density functional theory (DFT) calculations were performed with VASP 5.4.4.[17–20] A plane wave basis set with an energy cutoff of 700 eV with the projector augmented (PAW) potentials [21,22] was used. Thus only the valence electrons of Cu, Zn (both 4s and 3d), Ag, and Cd (both 5s and 4d) were explicitly considered. The electronic convergence criteria was set at least to 10^{-5} eV, whereby the Blocked-Davidson algorithm was applied as implemented in VASP. The structural relaxation of internal and external lattice parameters was set to a force convergence of 10^{-2} eV/Å^2 while the conjugate-gradient algorithm implemented in VASP was used.[23] The freedom of spin polarization was enabled and a Gaussian smearing approach with a smearing factor σ of 0.01 eV was utilized. For all fully ordered structures we simulated 16 atoms which corresponds to the number of atoms in the kesterite unit cell. The cells were fully optimized with a 8x8x4 (zincblende-type or GeSb-type structures) or 7x7x7 (wurtzite structures) k-grid constructed via the Monkhorst-Pack scheme[24] and centered at the Γ-point with the PBE functional.[25] On top of the PBE-optimized structures, single point calculations for the band gap and DOS with the HSE06-functional[26–29] were performed with a 4x4x2 (zinc blende-type or GeSb-type structures) or 4x4x4 (wurtzite-type structures) k-grid to account for an accurate electronic structure. The tetrahedron method with Blöchl corrections[30] was applied for the band structure evaluation. For the disordered KS structures we fully optimized 64 atoms (equivalent to a 2x2x1 kesterite super cell) using 4x4x4 k-grid.

The pressure dependence was determined by selecting volume points in a range of about

40 Å^3 above and below the minima. This corresponds to a pressure range of roughly 0-12 GPa. We used a step size of 4 Å^3 which lead to at least 24 volume points for each structural model. At each point we optimized the ionic positions and cell shape, while keeping the cell volume constant. We fitted the total energy versus volume to a Birch-Murnaghan Equation of State (B-M EoS).[31] Then the pressure at each volume was obtained from the *P(V)* formulation of the same EoS (for details see supporting information section S.3). For the B-M EoS fits of the low pressure structures we only use data points below the transition pressure, because above this pressure the structures start to deform significantly towards to the high pressure ones. We used at least 16 volume points per fit. Using the pressure we calculated the enthalpies ($H(P) = E + PV$) for each structural model and compared them over the investigated pressure range to identify the most stable structures.

Structural models

Ordered structures

In quaternary chalcogenide semiconductors the structure at equilibrium pressure in most cases are kesterite-type (KS, fig. 2 a), stannite-type (ST, fig. 2 b), wurtzkesterite-type (WZ-KS, fig. 2 c) or wurtzstannite-type (WZ-ST, fig. 2 d) structures.[32] KS and ST are derived from the zincblende-type (ZB) structure. WZ-KS and WZ-ST are derived from the wurtzite-type structure. For the WZ structures we use equivalent tetragonal unit cells, but be aware that the asymmetric unit is hexagonal. In the tetragonal representation of the WZ cell we can easily see the relation to the corresponding ZB derived structure. For instance, in WZ-KS the cationic arrangements in the *a*-*c*-planes are identical to the cationic arrangements in the *a*-*c*-planes in KS. The same relation holds for both ST structures. We include all mentioned structures as potential low pressure phases for Ag_2ZnSnS_4 and Ag_2CdSnS_4. In our high pressure study on KS Cu_2ZnSnS_4 we found the distorted rocksalt structure (GeSb-type, fig. 1 b) to be the most stable phase beyond 16 GPa. Therefore we also include the GeSb-type structure as a high pressure phase in this study. For the GeSb-type structure we

utilize two unit cells (stacked along c-axis), so that the number of atoms matches the KS unit cell.

All ZB and WZ derived structures have a coordination number of 4, due to the same structural motif they are close in formation energy and the structure formation is dependent on crystallization conditions. GeSb has a coordination number of 6, so this structure is fundamentally different from the four fold coordinated ZB and WZ structures. Transitioning from a four to a six fold coordination is a structural change associated with a large difference in the energy of formation.

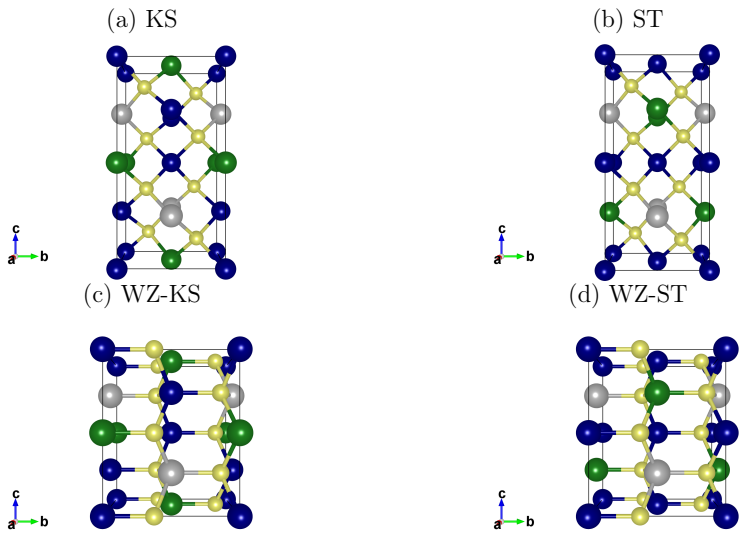

Figure 2: Structural models for the (a) kesterite-type (KS, $I\bar{4}$), (b) stannite-type (ST, $I\bar{4}2m$), (c) wurtzkesterite-type (WZ-KS, Pn), (d) wurtzstannite-type (WZ-ST, $Pmn2_1$) structure. Blue: Ag, Green: Zn/Cd, grey: Sn and yellow: S.

Disordered kesterite models

In Cu_2ZnSnS_4 (KS) Cu-Zn disorder is a common effect. The exchange is thought to only take place within the Cu-Zn-planes[14,33] and is promoted by the similar ionic radii. We classify disordered structures by their disorder fraction, which we define as the number of atoms

in the two Cu-Zn planes within the cell which have changed their place in comparison to the fully ordered KS structure divided by the total number of atoms of the planes. In the kesterite unit cell (fig. 1 a) there are four atoms within the two Cu-Zn planes. Exchanging two of them leads to a disorder fraction of 50 %. Disorder fractions above 50 % lead to the same structures as for the disorder fractions below due to the crystal symmetry.

The energies of all possible disorder patterns in a 2x2x1 super cell for Cu_2ZnSnS_4 were calculated to understand why disorder occurs easily and how it effects the band gap.[34,35] All possible 910 disorder patterns within this supercell have been investigated. In this study we want to compare Ag_2ZnSnS_4 and Ag_2CdSnS_4 to Cu_2ZnSnS_4 without calculating all patterns for each material. We selected 3 to 5 patterns for each disorder fraction (fig. S.4 and S.5 in supporting information) in such a way, that they span the whole energy range which occurs for Cu_2ZnSnS_4.[34,35]

Results and Discussion

Equilibrium structures

We start by reviewing the equilibrium structures of Ag_2ZnSnS_4 and Ag_2CdSnS_4 obtained at the PBE level (tab. 1) and relate them to other published results.

The mineral pirquitasite, in its ideal composition corresponding to Ag_2ZnSnS_4, was first characterized in 1982 by *Johan* and *Picot*. Based on their XRD (X-ray diffraction) measurements they concluded that Ag_2ZnSnS_4 must have a ST or KS structure.[36] The question which of the two ZB structures is more stable was answered in 2013 by *Schumer et al.*[37] Their XRD measurement indicated that Ag_2ZnSnS_4 has a KS structure at ambient pressure. Those results agree with DFT calculations by *Chen et al.*, which also predict the KS structure to be most stable.[32] In 2019 neutron diffraction measurements by *Mangelis et al.* proofed that ATZS has a KS structure.[38]

Our PBE calculations also predict the KS structure to be most stable (tab. 1). The

WZ-KS structure is only 19 meV less stable, followed by the WZ-ST structure and finally the ST structure. The PBE lattice parameters for KS match the experimental results,[38] a deviates by +0.4 % and c by −3 %, which we consider to be within the expected PBE error.

Table 1: Optimized lattice parameter a, b, c (in Å) and β (in °) for Ag_2BSnS_4 (B: Zn, Cd) KS, ST, WZ-KS and WZ-ST at the PBE level of theory in comparison to other simulated and experimental (exp.) results. ΔE denotes the energy difference per unit cell to the most stable phase (in meV).

B	KS			ST			WZ-KS					WZ-ST				
	a	c	ΔE	a	c	ΔE	a	b	c	β	ΔE	a	b	c	ΔE	Method
	5.835	11.088	0	5.564	12.177	293	6.665	6.922	8.197	89.98	32	7.831	7.200	6.695	172	PBE
Zn	5.812	10.779														exp.[38]
			0			298					19				162	PW91[32]
	5.910	11.560	0	5.803	11.975	95	6.807	7.150	8.303	90.07	0	8.147	7.260	6.820	40	PBE
Cd							6.704	7.037	8.217	90.16		8.217	7.064	6.703		exp.[39]
			14			117					0				38	PW91[32]

The crystal structure of Ag_2CdSnS_4 was first determined in the late 1960s by *Parthé* and *Deitch*. They assigned the space group $Cmc2_1$ based on their XRD results.[40] This assignment was confirmed in 2005 by *Parasyuk et al.*, again using XRD.[41] 2020 *Heppke et al.* carried out an *in-situ* XRD study at different temperatures.[39] They found a low and high temperature phase. For the low temperature phase occurring below 200°C they excluded the space group $Cmc2_1$ due to additional reflections in their XRD pattern. Instead they assigned WZ-KS. At 200°C they observed a first order phase transition to WZ-ST.

Also at the PBE level the WZ-KS structure is the most stable (tab. 1). But it is only 0.1 meV more stable than the KS structure, this energy difference is close to the accuracy of our calculations, so we cannot predict which of the two structures is more stable. The WZ-ST and ST structure are 38 and 117 meV less stable than the KS structures at the PBE level.

The DFT results are in agreement with the assignment of WZ-KS to the low temperature phase of Ag_2CdSnS_4 by *Heppke et al.*[39] The PBE lattice parameter for WZ-KS are within 1.5 % of the experimental results. For WZ-ST the deviations are similar, except for b where we observe a deviation of about 3 %. We consider this agreement to be within the error of

the applied functional.

The predicted relative stability at the PBE level for both materials closely matches the PW91 results by *Chen et al.*,[32] only the difference in energy between KS and WZ-KS is more pronounced. The WZ-KS structure is 14 meV more stable than KS at the PW91 level.

The similarity of the DFT results is not surprising as both DFT functionals are from the same class of functionals, they use a generalized gradient approximation (GGA) for the exchange-correlation potential.[25]

High pressure behavior

The high pressure behavior gives hints how the materials perform structurally in thin-layer solar cells, where compressive stress occurs. For instance in 300nm thin TiN films compressive stress can amount up to 4 GPa.[42] Plotting the enthalpies for Ag_2ZnSnS_4 (fig. 3a and b) and Ag_2CdSnS_4 (fig. 3c and d), we find that the KS structure stays most stable until 8.2 GPa and 4.7 GPa, respectively. At those pressures we predict a transition to the GeSb-type structure for both materials. This transition leads to a shrinking of the unit cell by 16 % for Ag_2ZnSnS_4 and 18 % for Ag_2CdSnS_4. In Ag_2ZnSnS_4 the low pressure stability is unambiguous, the energy difference from the most stable KS structure to the second most stable WZ-KS structure is constantly around 40 meV until the transition pressure, afterwards it decreases to eventually become less stable around 11 GPa which has no effect on the experimental findings, because it is well above the transition pressure to the GeSb-type structure. For Ag_2CdSnS_4 KS and WZ-KS the enthalpies are similar up to the transition pressure. The maximum difference is 3 meV at 2.8 GPa. We estimated the error in ΔH (for details see supporting information section S.4) and came to the conclusion that the differences in enthalpy between KS and WZ-KS are not significant up to the transition. Consequently we cannot decide which of the two structures is more stable at low pressures for Ag_2CdSnS_4. As mentioned above experimentally the WZ-KS structure is observed at low pressure.[39] At 6.4 GPa WZ-KS also becomes more stable in our calculations, but this cannot be observed

experimentally as it is beyond the transition pressure for the GeSb-type structure.

In Ag_2ZnSnS_4 the relative stability of all low pressure phases remains close to the stability at ambient conditions up to the the transition pressure. For Ag_2ZnSnS_4 ST and WZ-ST the energy difference to KS at the transition pressure is 30 and 40 meV smaller than at ambient pressure. In Ag_2CdSnS_4 the enthalpy of the ST phase is slowly decreasing from 100 meV to 80 meV above the KS enthalpy. The enthalpy of WZ-ST Ag_2CdSnS_4 decreases from 50 meV above KS at ambient pressure to become more stable around 6.5 GPa, which is beyond the transition pressure to the GeSb-structure.

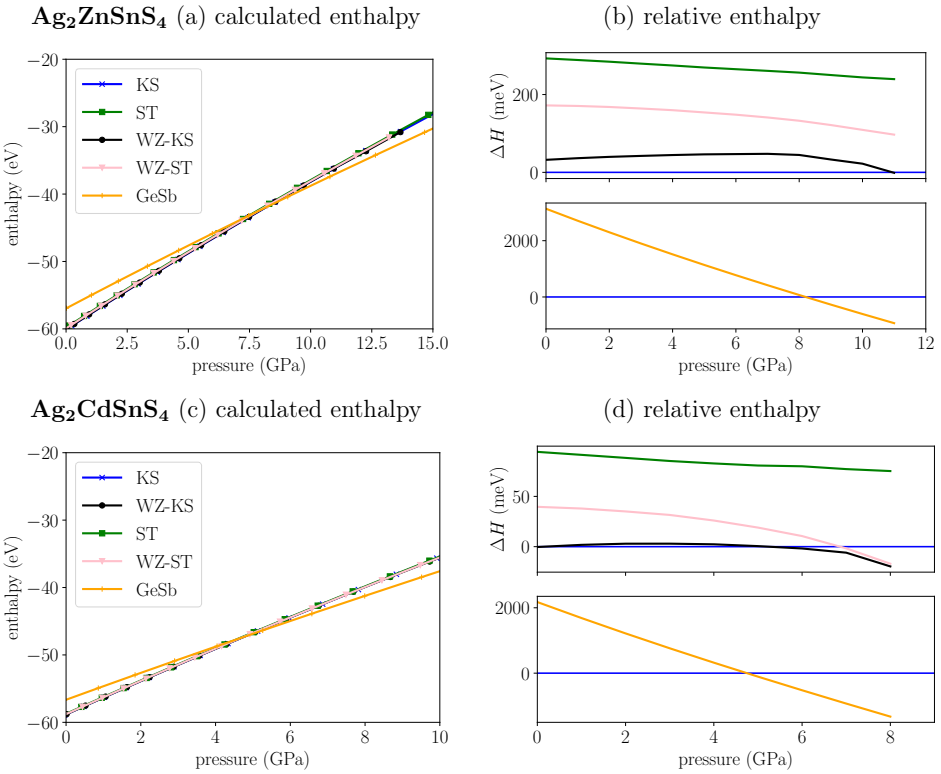

Figure 3: (a) and (c) PBE-calculated enthalpies for KS, ST, WZ-KS, WZ-ST and GeSb-type structural models as a function of pressure for Ag_2ZnSnS_4 and Ag_2CdSnS_4. Because the enthalpy differences are very small we also calculated relative enthalpy differences (b) and (d) with reference to the most stable structure for Ag_2ZnSnS_4 and Ag_2CdSnS_4.

Now we compare the predicted phase transitions for the two Ag KS/WZ-KS to the phase transition in Cu_2ZnSnS_4 (tab. 2). Exchanging Cu for Ag leads to a reduction of the transition pressure nearly by a factor of two. Additionally exchanging Zn for Cd leads to another 1.75-fold decrease of the transition pressure. The relative volume change due to the pressure induced transition however is within 3.1 % in all materials, so quite similar. With reference to the resistance against stress, we conclude that Ag_2ZnSnS_4 and Ag_2CdSnS_4 are significantly less resistant than Cu_2ZnSnS_4. Still Ag_2ZnSnS_4 seems suitable for the use in thin films solar cells as its transition pressure is two times larger than the maximum compressive stress of 4 GPa expected in thin films.[42] The transition pressure of Ag_2CdSnS_4, however, is only 0.7 GPa larger than the maximum compressive stress in thin films. We conclude that this could lead to unwanted structural changes in very thin Ag_2CdSnS_4 films.

Table 2: Predicted transitions for Ag_2ZnSnS_4 and Ag_2CdSnS_4 in comparison to experimental transition for Cu_2ZnSnS_4. The table contains the transition pressure (p_T in GPa) with the corresponding cell volumina before (V_1 in Å^3) and after (V_2 in Å^3) the transition, ΔV denotes the relative volume change.

Composition	p_T	transition	V_1	V_2	ΔV
Ag_2ZnSnS_4	8.2	KS $\rightarrow$ GeSb	337	282	-16.3 %
Ag_2CdSnS_4	4.7	WZ-KS/KS $\rightarrow$ GeSb	374	306	-18.0 %
Cu_2ZnSnS_4[8]	16.0	KS $\rightarrow$ GeSb	280	240	-15.2 %

We want to analyze how the bulk modulus changes due to the phase transitions in the materials Ag_2ZnSnS_4 and Ag_2CdSnS_4 and compare to Cu_2ZnSnS_4. We do that based on the B-M.-EOS fit coefficients as the bulk modulus and its first derivative are variables in the EOS. The bulk moduli of the low pressure structures amount to 81 % for Ag_2ZnSnS_4 and 73/75 % for Ag_2CdSnS_4 of the bulk modulus of KS Cu_2ZnSnS_4 (Tab. 3). Comparing the different materials at low pressure the bulk moduli reflect the different transition pressures. The lower the bulk modulus, the lower the transition pressure. The bulk moduli of the GeSb-type high pressure structures amount to 92 % for Ag_2ZnSnS_4 and 88 % for Ag_2CdSnS_4 of the bulk modulus of GeSb-type Cu_2ZnSnS_4. The first derivative of the bulk modulus is within

10 % for all materials and structures. For all materials $B_0^{'}$ of the GeSb-type structure is smaller than for the low pressure phases.

Table 3: PBE bulk modulus (B_0 in GPa) and first derivative ($B_0^{'}$) for the listed structural models (Struc.) for the listed compositions. Derived from the Birch–Murnaghan EoS fit. For all fit paramters please refer to supporting info section S.3.

Composition	Struc.	B_0	$B_0^{'}$
Ag_2ZnSnS_4	KS	54.71	4.96
Ag_2ZnSnS_4	GeSb	75.84	4.68
Ag_2CdSnS_4	WZ-KS	49.50	5.10
Ag_2CdSnS_4	KS	50.69	5.20
Ag_2CdSnS_4	GeSb	71.72	4.83
Cu_2ZnSnS_4 [8]	KS	68.63	4.64
Cu_2ZnSnS_4 [8]	GeSb	82.16	4.57

Electronic structure at ambient and high pressure

For the use as solar cell absorber the size of the band gap is crucial. Therefore we investigated the electronic band structure for equilibrium and high-pressure structures for both compounds with the HSE06 hybrid functional.[26]

The results for the band gap at equilibrium pressure for KS Ag_2ZnSnS_4 and WZ-KS Ag_2ZnSnS_4 are very similar. In both cases we predict a band gap of 1.5 eV (tab. 4). The experimentally observed band gaps are 2.0 eV[43] and 1.93 eV.[39] Considering that HSE06 usually gives very accurate band gaps, the deviation of 0.5 eV seems large. We are confident that the reason for the large deviation is mainly that we did not optimise our structures at the HSE06 level but only with PBE. We have encountered this phenomena before when studying Cu_2ZnSnS_4.[35] In Cu_2ZnSnS_4 the HSE band gap of the PBE optimized structure is 1.2 eV. If we also optimize with HSE06 the band gap increases to 1.5 eV. Having this in mind, we think that our HSE06 band gaps are reasonably close to the experimental results.

To test if the band gap is a suitable criterion to distinguish the different structures for each material, we also calculated the band gaps for all other structural models (tab. 4).

For Ag_2ZnSnS_4 we predict the band gaps of all structures within an interval of 0.3 eV, for Ag_2CdSnS_4 the interval is 0.4 eV. Within those intervals the differences between the structures are 0.1 or 0.2 eV. We consider those differences as too small to distinguish them based on experimental band gaps. The reason for the similar band gaps is that all ZB and WZ structures have a tetrahedral binding motif around sulfur anions, therefore the chemical bonding situation is similar and also the resulting DOS (see supporting information S.7.2).

Table 4: Calculated HSE06 band gaps (single point calculations for the optimized PBE structures) E_g (in eV) for Ag_2CdSnS_4 and Ag_2CdSnS_4 for the listed strucutral models (struc.) in comparison to experimental (exp.) results.

Composition	Struc.	E_g	exp.
Ag_2ZnSnS_4	KS	1.5	2.0[43]
Ag_2ZnSnS_4	WZ-KS	1.6	-
Ag_2ZnSnS_4	WZ-ST	1.4	-
Ag_2ZnSnS_4	ST	1.2	-
Ag_2CdSnS_4	WZ-KS	1.5	1.93[39]
Ag_2CdSnS_4	WZ-ST	1.3	-
Ag_2CdSnS_4	KS	1.4	-
Ag_2CdSnS_4	ST	1.2	-

To analyze how the electronic structure changes due to the pressure induced transition, we calculated the DOS at the transition pressure for the low and high pressure structure for Ag_2ZnSnS_4 and Ag_2CdSnS_4 (fig. 4). The results for both materials are very similar, we find that the band gap in KS or WZ-KS closes completely after the transition to GeSb. We observe that all bands from the valence band now extend in the region from 0 eV to 1.5 eV which is the band gap region for the KS or WZ-KS structure. The electronic structure changes from semiconducting to metallic for both materials. Before the transition the band gap in KS Ag_2ZnSnS_4 widens by 0.2 eV in comparison to equilibrium pressure. For Ag_2CdSnS_4 we plotted the DOS for the WZ-KS for the low pressure phase because the XRD experiments by *Heppke et al.*[39] indicate it as the equilibrium pressure structure. For Ag_2CdSnS_4 WZ-KS the band gap does not widen prior to the transition. We suspect that is because the transition takes place at a 3 GPa lower pressure than in KS Ag_2ZnSnS_4. We are confident that the

results would be the same if we used a KS Ag_2CdSnS_4 low pressure phase because the DOS are nearly identical at equilibrium pressure.

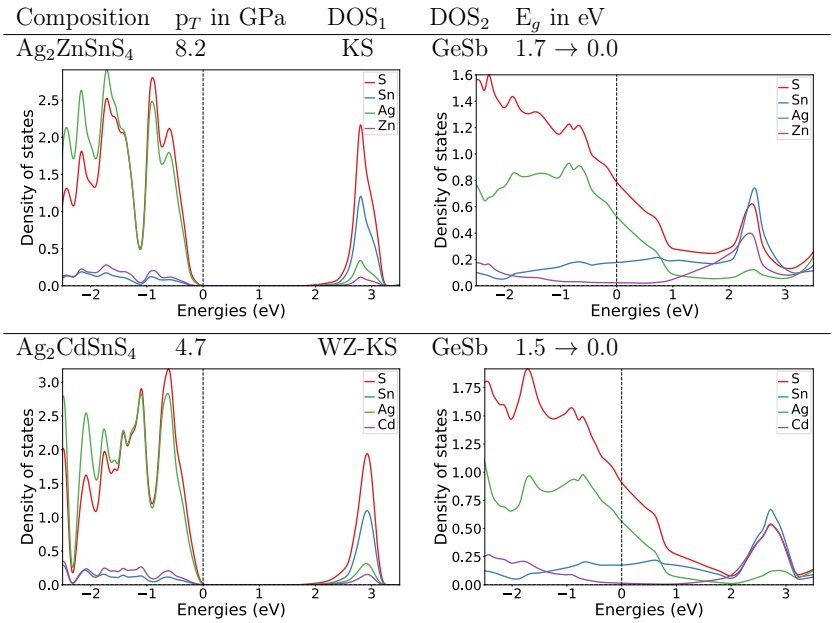

Figure 4: DOS plots at the transition pressure at the HSE06 level for the listed pressure induced transitions for Ag_2ZnSnS_4 and Ag_2CdSnS_4

Disorder

We restrict our investigations to the KS structure, because it is the most stable phase for Ag_2ZnSnS_4 and Cu_2ZnSnS_4. Although the situation is not as defined as in Ag_2CdSnS_4, also there the KS structure is one of the two possibilities of the low pressure phases. Also it can give an indication how doping KS Cu_2ZnSnS_4 with Ag and Cd together[12] influences disorder.

To predict how sensitive the materials Ag_2ZnSnS_4 and Ag_2CdSnS_4 are towards disorder, we calculated at least three disordered structures for each disorder fraction within 2x2x1 super cells. The relative energies with respect to the ideal KS structure (fig. 5 a and b) are compared to the ones of Cu_2ZnSnS_4 (fig. S.6 in supporting information). It strikes that the

results for Ag_2CdSnS_4 and Cu_2ZnSnS_4 are nearly identical with relative energies ranging from 20 to 270 meV. The relative energy order of the patterns within each disorder fraction is the same, except for small deviations for the disorder fraction of 37.5 % and 50 %. Also the relative energies themselves for each pattern are similar in Ag_2CdSnS_4 and Cu_2ZnSnS_4. Also it strikes that in both materials there is a disorder pattern with 50 % disorder (pattern (a), fig. S.5 in supporting information) which is less than 20 meV above the ideal KS. In this pattern (space group $P\bar{4}2c$) both Ag-Cd planes are symmetrical with respect to the middle Ag-Sn plane of the cell. This pattern is very similar to KS itself, as it can be obtained by rotating the lower half of the KS unit cell (fig. 2 a) by 90° (or by switching Ag and Cd in the lower Ag-Cd plane). For Ag_2CdSnS_4 and Cu_2ZnSnS_4 there are 5 disorder patterns with relative energies under 100 meV including pattern (a) at 50 % disorder fraction which is nearly as stable as ideal KS.

For Ag_2ZnSnS_4 all relative energies are higher than for the other two, ranging from 100 to 400 meV. For the disorder fractions 25.0 %, 37.5 % and 50 % the order of the patterns is different than for Cu_2ZnSnS_4 and Ag_2CdSnS_4. Some patterns get significantly destabilized in comparison to the other two materials, those are pattern (a) and (c) at 25.0 % disorder fraction, pattern (c) at 37.5 % disorder fraction and patterns (a), (c) and (d) at 50 % disorder fraction.

Cu_2ZnSnS_4 is known to be affected by cationic disorder and based on the relative energies of the disordered structures we expect the same for Ag_2CdSnS_4. All disordered structures for Ag_2ZnSnS_4, however, are at least 100 meV above ideal KS and therefore we predict that this material is much less sensitive to disorder than the other two. DFT calculations for Ag_2ZnSnS_4 by *Mangelis et al.* where only five disorder patterns were considered indicate the same result.[38]

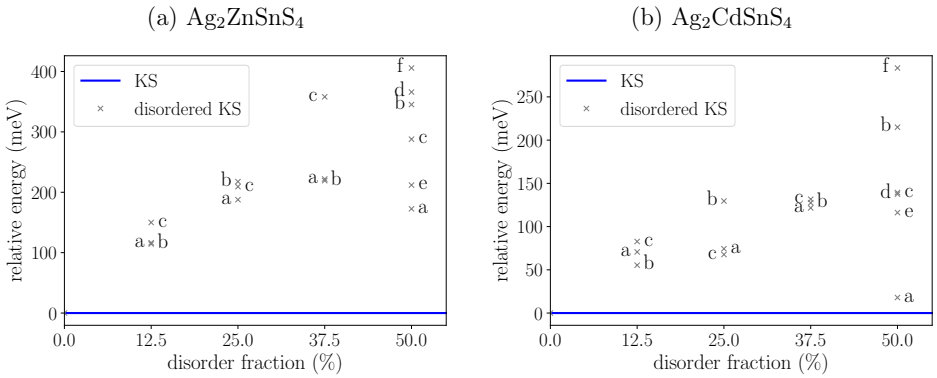

Figure 5: Relative PBE energies of disordered KS structures with reference to ideal KS for a) Ag_2ZnSnS_4 and b) Ag_2CdSnS_4.[13] For Cu_2ZnSnS_4 please refer to fig. S.6 in supporting information.

Summary and conclusions

We simulated the enthalpies for different structural models for Ag_2ZnSnS_4 and Ag_2CdSnS_4 to identify low and high pressure modifications. In agreement with experimental results, we found the tetrahedrally coordinated KS structure to be the most stable for Ag_2ZnSnS_4 at equilibrium pressure. At 8.2 GPa we predict a transition to the six-fold coordinated GeSb structure. This is accompanied by a change of the electronic structure from semiconducting to metallic. For Ag_2CdSnS_4 the situation is not so clear. Numerically we get the same result as *Heppke et al.* in their XRD measurements at low temperature,[39] that WZ-KS is most stable. The difference to the next least stable KS structure is only 0.1 meV, which we consider too small in comparison to the error of our calculations to determine which structure is more stable. Beyond 4.7 GPa we found the GeSb-type structure to be undoubtedly as the most stable one. The transition also leads to a change of the electronic structure from semi-conducting to metallic. Also in Cu_2ZnSnS_4 we find a metallic GeSb-type high pressure phase, the transition pressure of 16 GPa, however, is larger by a factor of two for Ag_2ZnSnS_4 and three for Ag_2CdSnS_4.

Compressive stress in thin films can amount up to 4 GPa in TiN films.[42] Assuming

similar behavior for thin films of the investigated materials, we conclude that Ag_2ZnSnS_4 and Cu_2ZnSnS_4 are sufficiently resistant to compressive stress. The transition pressure of Ag_2CdSnS_4 is close to the maximum compressive stress in TiN thin films, therefore it could become critical for the usage in very thin films. If the WZ-KS or KS to GeSb-type transition is triggered, the material is rendered useless as a solar cell absorber, due to the metallic electronic structure of the GeSb-type structure.

By calculating differently disordered KS patterns we also revealed that KS Ag_2CdSnS_4 is similarly prone to disorder as KS Cu_2ZnSnS_4. The reason is that the ionic radii of Cu^+ and Zn^{2+} are relatively similar as well as the ionic radii of Ag^+ and Cd^{2+}. Those elements constitute two planes in the KS unit cell which can easily get disordered if the elements are similar in size. In Ag_2ZnSnS_4 the effective ionic radii of the elements are sufficiently different for the disordered structures to be destabilized by 50 to 150 meV each in comparison to Cu_2ZnSnS_4 and Ag_2CdSnS_4. We conclude that Ag_2ZnSnS_4 is much less sensitive to disorder.

Acknowledgement

The authors acknowledge the North-German Supercomputing Alliance (HLRN) for providing HPC (high performance computing) resources that have contributed to the research results reported in this paper. Financial support from International Max Planck Research School (IMPRS) Functional Interfaces in Physics and Chemistry is gratefully acknowledged.

Supporting Information Available

The following files are available free of charge.

- Ag_KS_supporting_information.pdf: all DFT energies and structural data, BM-fit parameter, error estimation ΔH, additional DOS, disordered KS models, CZTS data for comparison

References

(1) Tanaka, T.; Nagatomo, T.; Kawasaki, D.; Nishio, M.; Guo, Q.; Wakahara, A.; Yoshida, A.; Ogawa, H. Preparation of Cu_2ZnSnS_4 thin films by hybrid sputtering. *Journal of Physics and Chemistry of Solids* **2005**, *66*, 1978–1981.

(2) Scragg, J. J.; Dale, P. J.; Peter, L. M.; Zoppi, G.; Forbes, I. New routes to sustainable photovoltaics: Evaluation of Cu_2ZnSnS_4 as an alternative absorber material. *Physica Status Solidi (B) Basic Research* **2008**, *245*, 1772–1778.

(3) Giraldo, S.; Jehl, Z.; Placidi, M.; Izquierdo-Roca, V.; Pérez-Rodríguez, A.; Saucedo, E. Progress and Perspectives of Thin Film Kesterite Photovoltaic Technology: A Critical Review. *Advanced Materials* **2019**, *31*, 1806692.

(4) Yan, C. et al. Cu_2ZnSnS_4 solar cells with over 10% power conversion efficiency enabled by heterojunction heat treatment. *Nature Energy* **2018**, *3*, 764–772.

(5) Wang, W.; Winkler, M. T.; Gunawan, O.; Gokmen, T.; Todorov, T. K.; Zhu, Y.; Mitzi, D. B. Device characteristics of CZTSSe thin-film solar cells with 12.6% efficiency. *Advanced Energy Materials* **2014**, *4*, 1–5.

(6) Janssen, G. C. Stress and strain in polycrystalline thin films. *Thin Solid Films* **2007**, *515*, 6654–6664.

(7) Taylor, P.; Presser, V.; Nickel, K. G. Critical Reviews in Solid State and Materials Sciences Silica on Silicon Carbide Silica on Silicon Carbide. *Crtitical Reviews in Solid State and Matrials Sciences* **2008**, 37–41.

(8) Efthimiopoulos, I.; Küllmey, T.; Speziale, S.; Pakhomova, A. S.; Quennet, M.; Paulus, B.; Ritscher, A.; Lerch, M.; Koch-Müller, M. Pressure-induced structural and electronic transitions in kesterite-type Cu_2ZnSnS_4. *Journal of Applied Physics* **2018**, *124*, 085905.

(9) Ma, C.; Guo, H.; Zhang, K.; Li, Y.; Yuan, N.; Ding, J. The preparation of Ag_2ZnSnS_4 homojunction solar cells. *Materials Letters* **2017**, *207*, 209–212.

(10) Guo, H.; Ma, C.; Zhang, K.; Jia, X.; Li, Y.; Yuan, N.; Ding, J. The fabrication of Cd-free Cu_2ZnSnS_4-Ag_2ZnSnS_4 heterojunction photovoltaic devices. *Solar Energy Materials and Solar Cells* **2018**, *178*, 146–153.

(11) Saha, U.; Alam, M. K. Boosting the efficiency of single junction kesterite solar cell using Ag mixed Cu_2ZnSnS_4 active layer. *RSC Advances* **2018**, *8*, 4905–4913.

(12) Gershon, T.; Lee, Y. S.; Antunez, P.; Mankad, R.; Singh, S.; Bishop, D.; Gunawan, O.; Hopstaken, M.; Haight, R. Photovoltaic materials and devices based on the alloyed kesterite absorber $(Ag_xCu_{1-x})_2Zn(Sn,Se)_4$. *Advanced Energy Materials* **2016**, *6*, 1–7.

(13) Quennet, M.; Ritscher, A.; Lerch, M.; Paulus, B. The order-disorder transition in Cu_2ZnSnS_4: A theoretical and experimental study. *Journal of Solid State Chemistry* **2017**, *250*, er.

(14) Scragg, J. J. S.; Larsen, J. K.; Kumar, M.; Persson, C.; Sendler, J.; Siebentritt, S.; Platzer Björkman, C. Cu-Zn disorder and band gap fluctuations in Cu2ZnSn(S,Se)4: Theoretical and experimental investigations. *Physica Status Solidi (B) Basic Research* **2016**, *253*, 247–254.

(15) Shannon, R. D. Revised effective ionic radii and systematic studies of interatomic distances in halides and chalcogenides. *Acta Crystallographica Section A* **1976**, *32*, 751–767.

(16) Ma, C.; Guo, H.; Zhang, K.; Yuan, N.; Ding, J. Fabrication of p-type kesterite Ag_2ZnSnS_4 thin films with a high hole mobility. *Materials Letters* **2017**, *186*, 390–393.

(17) Kresse, G.; Hafner, J. Ab initio molecular dynamics for liquid metals. *Physical Review B* **1993**, *47*, 558–561.

(18) Kresse, G.; Hafner, J. Ab initio molecular-dynamics simulation of the liquid-metal–amorphous-semiconductor transition in germanium. *Physical Review B* **1994**, *49*, 14251–14269.

(19) Kresse, G.; Furthmüller, J. Efficient iterative schemes for ab initio total-energy calculations using a plane-wave basis set. *Physical Review B* **1996**, *54*, 11169–11186.

(20) Kresse, G.; Furthmüller, J. Efficiency of ab-initio total energy calculations for metals and semiconductors using a plane-wave basis set. *Computational Materials Science* **1996**, *6*, 15–50.

(21) Blöchl, P. Projector augmented-wave method. *Physical Review B* **1994**, *50*, 17953–17979.

(22) Kresse, G.; Joubert, D. From ultrasoft pseudopotentials to the projector augmented-wave method. *Physical Review B* **1999**, *59*, 1758–1775.

(23) Press, W. H.; Flannery, B. P.; Teukolsky, S. A.; Vetterling, W. T.; Kramer, P. B. Numerical Recipes: The Art of Scientific Computing. *Physics Today* **1987**, *40*, 120–122.

(24) Monkhorst, H. J.; Pack, J. D. Special points for Brillouin-zone integrations. *Physical Review B* **1976**, *13*, 5188–5192.

(25) Perdew, J. P.; Burke, K.; Ernzerhof, M. Generalized Gradient Approximation Made Simple. *Physical Review Letters* **1996**, *77*, 3865–3868.

(26) Heyd, J.; Scuseria, G. E.; Ernzerhof, M. Hybrid functionals based on a screened Coulomb potential. *The Journal of Chemical Physics* **2003**, *118*, 8207–8215.

(27) Heyd, J.; Scuseria, G. E. Efficient hybrid density functional calculations in solids: Assessment of the Heyd–Scuseria–Ernzerhof screened Coulomb hybrid functional. *The Journal of Chemical Physics* **2004**, *121*, 1187–1192.

(28) Heyd, J.; Scuseria, G. E.; Ernzerhof, M. Erratum: "Hybrid functionals based on a screened Coulomb potential" [J. Chem. Phys. 118, 8207 (2003)]. *The Journal of Chemical Physics* **2006**, *124*, 219906.

(29) Krukau, A. V.; Vydrov, O. A.; Izmaylov, A. F.; Scuseria, G. E. Influence of the exchange screening parameter on the performance of screened hybrid functionals. *The Journal of Chemical Physics* **2006**, *125*, 224106.

(30) Blöchl, P. E.; Jepsen, O.; Andersen, O. Improved tetrahedron method for Brillouin-zone integrations. *Physical Review B* **1994**, *49*, 16223–16233.

(31) Birch, F. Finite Elastic Strain of Cubic Crystals. *Physical Review* **1947**, *71*, 809–824.

(32) Chen, S.; Walsh, A.; Luo, Y.; Yang, J. H.; Gong, X. G.; Wei, S. H. Wurtzite-derived polytypes of kesterite and stannite quaternary chalcogenide semiconductors. *Physical Review B - Condensed Matter and Materials Physics* **2010**, *82*, 1–8.

(33) Bourdais, S.; Choné, C.; Delatouche, B.; Jacob, A.; Larramona, G.; Moisan, C.; Lafond, A.; Donatini, F.; Rey, G.; Siebentritt, S.; Walsh, A.; Dennler, G. Is the Cu/Zn Disorder the Main Culprit for the Voltage Deficit in Kesterite Solar Cells? *Advanced Energy Materials* **2016**, *6*, 1–21.

(34) Quennet, M.; Ritscher, A.; Lerch, M.; Paulus, B. The order-disorder transition in Cu_2ZnSnS_4 : A theoretical and experimental study. *Journal of Solid State Chemistry* **2017**, *250*, 140–144.

(35) Marcel Quennet, First Principles Calculations for the Semiconductor Material Kesterite Cu_2ZnSnS_4 and Se-containing Derivatives. Ph.D. thesis, Freie Universität Berlin, 2016.

(36) Johan, Z.; Picot, P. La pirquitasite, Ag_2ZnSnS_4, un nouveau membre du groupe de la stannite. *Bulletin de Mineralogie* **1982**, *105*, 229–235.

(37) Schumer, B. N.; Downs, R. T.; Domanik, K. J.; Andrade, M. B.; Origlieri, M. J. Pirquitasite, Ag_2ZnSnS_4. *Acta Crystallographica Section E: Structure Reports Online* **2013**, *69*, 2–7.

(38) Mangelis, P.; Aziz, A.; Da Silva, I.; Grau-Crespo, R.; Vaqueiro, P.; Powell, A. V. Understanding the origin of disorder in kesterite-type chalcogenides A_2ZnBQ_4 (A = Cu, Ag; B = Sn, Ge; Q = S, Se): The influence of inter-layer interactions. *Physical Chemistry Chemical Physics* **2019**, *21*, 19311–19317.

(39) Heppke, E. M.; Berendts, S.; Lerch, M. Crystal structure of mechanochemically synthesized Ag_2CdSnS_4. *Zeitschrift für Naturforschung B* **2020**, *75*, 393–402.

(40) Parthé, E.; Yvon, K.; Deitch, R. H. The crystal structure of Cu_2CdGeS_4 and other quaternary normal tetrahedral structure compounds . *Acta Crystallographica Section B Structural Crystallography and Crystal Chemistry* **1969**, *25*, 1164–1174.

(41) Parasyuk, O. V.; Olekseyuk, I. D.; Piskach, L. V.; Volkov, S. V.; Pekhnyo, V. I. Phase relations in the Ag_2S-CdS-SnS_2 system and the crystal structure of the compounds. *Journal of Alloys and Compounds* **2005**, *399*, 173–177.

(42) Köstenbauer, H.; Fontalvo, G. A.; Kapp, M.; Keckes, J.; Mitterer, C. Annealing of intrinsic stresses in sputtered TiN films: The role of thickness-dependent gradients of point defect density. *Surface and Coatings Technology* **2007**, *201*, 4777–4780.

(43) Gong, W.; Tabata, T.; Takei, K.; Morihama, M.; Maeda, T.; Wada, T. Crystallographic and optical properties of $(Cu,Ag)_2ZnSnS_4$ and $(Cu,Ag)_2ZnSnSe_4$ solid solutions. *Physica Status Solidi (C) Current Topics in Solid State Physics* **2015**, *12*, 700–703.

3.5 Paper E

"Experimental and theoretical investigations on the composition-dependent structural phase transition in $Cu_2Cd_xZn_{1-x}SnS_4$"

Heppke, E. M., Küllmey, T., Efthimiopoulos, I., Avci, F. D., Appelt, O., Paulus, B. and Lerch, M., *Mater. Res. Express* **2019**, *6*(12), 1125525

DOI: 10.1088/2053-1591/ab59a0

URL: `http://www.doi.org/10.1088/2053-1591/ab59a0`

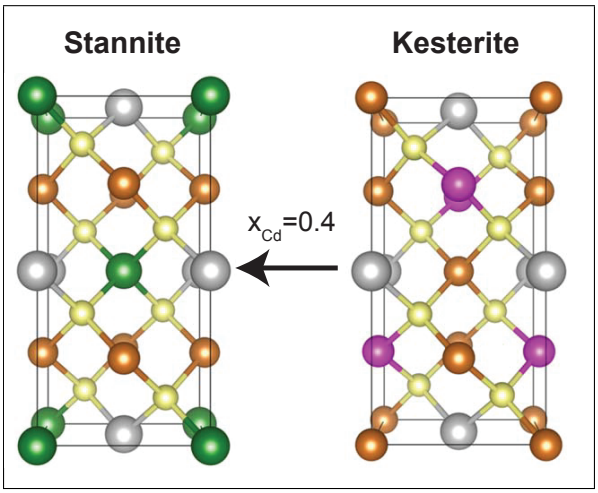

Graphical abstract of Paper E.

Contributions: The concept for this paper was developed by E.H. The experiments where conducted by E.H., F.A and O.A. All DFT calculation and subsequent data analysis was carried out by T.K. The initial draft of the paper was written by E.H. and T.K. Editing was done by E.H. with input from all other authors. The whole project was supervised by M.L and B.P.

4 Summary

In this chapter all publication included in this thesis will be summarized and discussed in relation to each other. Four papers deal with high-pressure behavior of ideal (**paper A**) and disordered Cu_2ZnSnS_4 (**paper B**) and substituted CZTS materials (**paper C**: $Ag_2(Zn/Cd)SnS_4$, **paper D**: $Cu_2(Mn/Fe)SnS_4$). They will be discussed together with the aim of pointing out the differences arising from the substitution. The final **paper E** deals with a structural transition in the solid solution series $Cu_2Zn_{1-x}Cd_xSnS_4$. The **papers A**, **B** and **E** are joined experimental and theoretical studies, the **papers C** and **D** are theoretical studies.

The research question we aimed to answer in the **papers A** to **D** is when and how does the crystal structure of the equilibrium phase of a potential KS solar cell material change under compressive stress. In thin-film technologies featuring sputtering on substrates compressive stress up to 3 GPa can occur.[43,44] Also the KS absorber or other layers of the kesterite solar cell like the CdS buffer layer can be sputtered. In that context it is important to understand what happens to the absorber material at higher pressure. If the electronic structure is no longer of semi-conducting character the structural change limits the pressure range in which the solar cell absorber material functions as such. The reason we also investigate four cation substituted CZTS materials is that those substitutions are introduced in the hope of solving the biggest issue of the KS solar cell, the V_{OC} deficit.[17]

Before attempting to predict the high-pressure phases we calculated the equilibrium structures at zero pressure and compared to experimental results to verify that our calculations give reasonable results. For each composition we tested various structural models (see selected examples in fig. 4.1) always including the kesterite-type structure (fig. 4.1a) and the experimentally most stable structure.

Experimentally disordered kesterite exhibits $I\bar{4}2m$ symmetry (fig. 4.2a), that means that at every position in the Cu-Zn planes (framed blue) the probability to find Cu and Zn is equally 0.5. Representing the disordered kesterite phase in a computational model is difficult because multiple substitution patterns need to be taken into account, and the number grows rapidly with the unit cell size. In our study we chose to use the most simple model for disordered kesterite, which can be derived directly from the KS unit cell only using one substitution pattern. We exchange one of the two Cu-Zn pairs in a plane, which gives rise to a $P\bar{4}2c$ symmetric structure (fig. 4.2b) we refer to as DKS. In this structure the number of disordered atoms in the planes is 2 out of 4 which means it is 50 % disordered just like the $I\bar{4}2m$ structure.

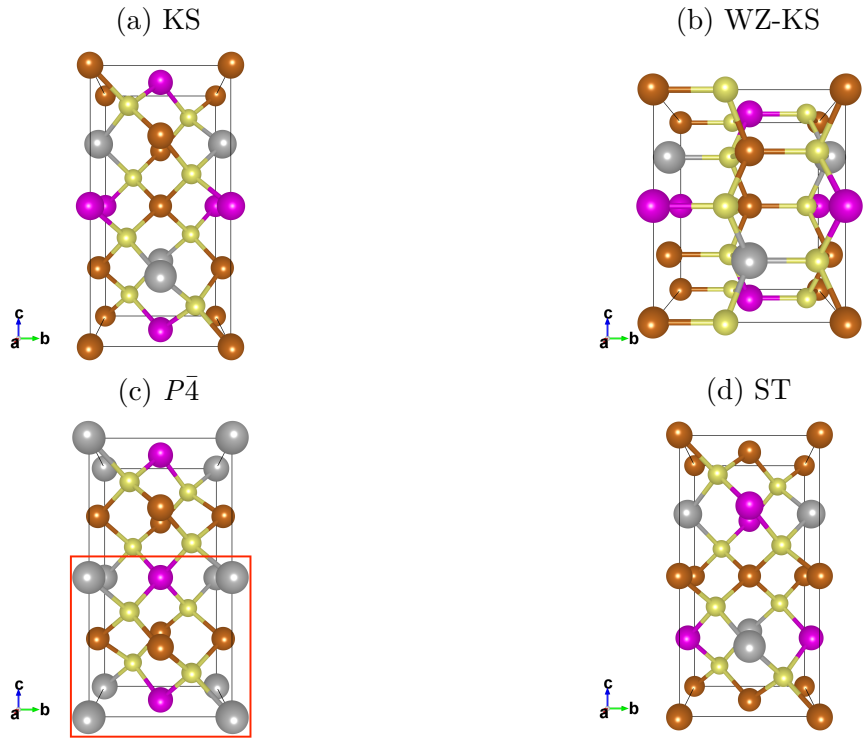

Figure 4.1: Four-fold coordinated structural models for the equilibrium phases: (a) kesterite-type (KS, $I\bar{4}$), (b) wurtzkesterite-type (WZ-KS, Pn), (c) $P\bar{4}$ and (d) stannite-type (ST, $I\bar{4}2m$) structure. Copper: Ag/Cu, pink: Zn/Cd/Fe/Mn, grey: Sn and yellow: S. In the $P\bar{4}$ structure the unit cell is highlighted in red, it is only half the size of the others.

In **paper D** we treat materials which contain the magnetic ions Mn^{2+} or Fe^{2+}. The unit cells we use contain two of those magnetic ions. We exploit that to model two different magnetic phases. In the ferromagnetic (FM) phase the magnetic moments of the two Mn^{2+} or Fe^{2+} ions are set to be parallel. For the anti-ferromagnetic (AM) case the magnetic moments are set antiparallel. We tested both magnetic phases for all structural models to find the most stable structural and magnetic phase.

We found a high level of agreement between our PBE calculations and experimental findings (tab. 4.1). For four out of five material compositions the PBE results predict the experimental equilibrium structure to be most stable. Only for Cu_2MnSnS_4 PBE predicts kesterite-type to be more stable when experimentally the stannite-type (ST, fig. 4.1a) structure is observed. The energy difference between KS and ST at the PBE level is 22 meV, so numerically the error is relatively small. For Ag_2CdSnS_4 PBE does correctly predict the experimental equilibrium structure WZ-KS to be most stable. But it is only 0.1 meV more stable than KS. When testing which K-Point grid size is required we converge the energies to 1 meV or less. This determines the accuracy of our calculations and a difference of 0.1 meV is close to that threshold and consequently we consider the KS and WZ-KS structures to be equally stable at the PBE level. The PBE lattice parameter of KS and DKS are nearly identical, which can be explained by the fact that only one Cu-Zn exchange is necessary to transition between the two structures.

Figure 4.2: Structural models for disordered kesterite (DKS) (a) $I\bar{4}2m$ symmetric and (b) $P\bar{4}2c$ symmetric. Copper: Cu, pink: Zn, grey: Sn and yellow: S.

The largest error in the predicted lattice constants can be found for lattice parameter c for Ag_2ZnSnS_4, which is +2.9 %. The average error for lattice constants of solids for PBE is 1.2 %, the maximum error in the test set used by *Zhang et al.* is 2.8 %.[75] We conclude that the deviation of the lattice parameters for all structures is within the expected error for the used functional.

Table 4.1: Most stable experimental (exp.) and PBE structures (struc.) at equilibrium pressure for the listed compositions (comp.) and corresponding lattice parameters a, b and c (in Å). SG stands for space group, AM denotes anti-ferromagnetic.

Comp.	PBE					exp.					
	struc.	SG	a	b	c	struc.	SG	a	b	c	source
Cu_2ZnSnS_4	KS	$I\bar{4}$	5.465	5.465	10.913	KS	$I\bar{4}$	5.431	5.431	10.855	**paper A**
Cu_2ZnSnS_4	DKS	$P\bar{4}2c$	5.465	5.465	10.924	DKS	$I\bar{4}2m$	5.457	5.457	10.901	**paper B**
Ag_2ZnSnS_4	KS	$I\bar{4}$	5.835	5.835	11.088	KS	$I\bar{4}$	5.812	5.812	10.779	[76]
Ag_2CdSnS_4	WZ-KS	Pn	6.807	7.150	8.303	WZ-KS	Pn	6.704	7.037	8.217	[77]
Cu_2FeSnS_4	(AM)	$P\bar{4}$	5.469	5.469	5.346	(AM)	$P\bar{4}$	5.433	5.433	5.410	[78]
Cu_2MnSnS_4	KS(AM)	$I\bar{4}$	5.468	5.468	11.020	ST(AM)	$I\bar{4}2m$	5.517	5.517	10.806	[79]

From the substituted CZTS structures only Ag_2ZnSnS_4 also crystallizes in the KS structure which is beneficial for the use in the kesterite solar cell system. It means silver substitution of Cu is possible in in every extend without changing the KS structure. Additional substitution of Zn by Cd stabilizes the WZ-KS structure, so there is a structural change which has to be avoided in KS solar cell absorbers. Also if Fe or Mn is used to substitute Zn in CZTS, the structure changes at some substitution fraction $\chi_{Fe/Mn}$ and this change has to be avoided in KS solar sell absorbers. For $Cu_2Zn_{1-x}Fe_xSnS_4$ the transition is predicted to be at $\chi_{Fe} = 0.40$ at the PBE level.[80] For the Mn substituted analogue no published data is available and we recommend to investigate this problem in the future.

For CZTS we chose the high-pressure structure based on the experimental high-pressure XRD (x-ray diffraction) results. Our collaborators found the GeSb-type structure (fig. 4.3a) to be most stable at high pressures. This structure has a coordination number of 6 for all ions. It is a compressed rocksalt structure, so c is slightly smaller than a and b (which are

equal). The KS structure can be derived from the sphalerite (ZnS) structure. ZnS exhibits a high temperature phase transition from sphalerite to wurtzite-type at about 1000°C.[81] To challenge the experimental results we also include the four-fold coordinated wurtzite-type (WZ, fig. 4.3b) structure as a potential high-pressure phase.

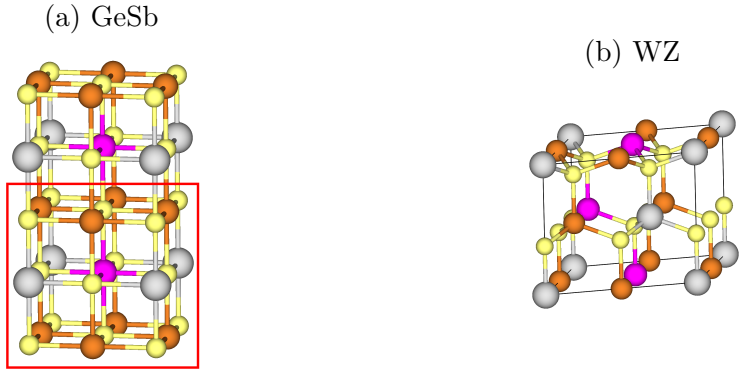

Figure 4.3: Tested CZTS high-pressure phases (a) GeSb-type ($I4/mmm$) and (b) wurtzite-type (WZ, $P2_1$). Copper: Cu, pink: Zn, grey: Sn and yellow: S. For the GeSb-type structure the unit cell is highlighted in red.

Fig. 4.4a shows the PBE enthalpies of the different tested structural models for Cu_2ZnSnS_4. Because the enthalpies are similar it is visually more clear to plot the enthalpies relative to the equilibrium KS phase (fig. 4.4b). The WZ enthalpy never gets the lowest, so it can not be observed experimentally. KS presents the most stable phase at low pressures. At 16 GPa we observe a structural transition to the GeSb-type phase.

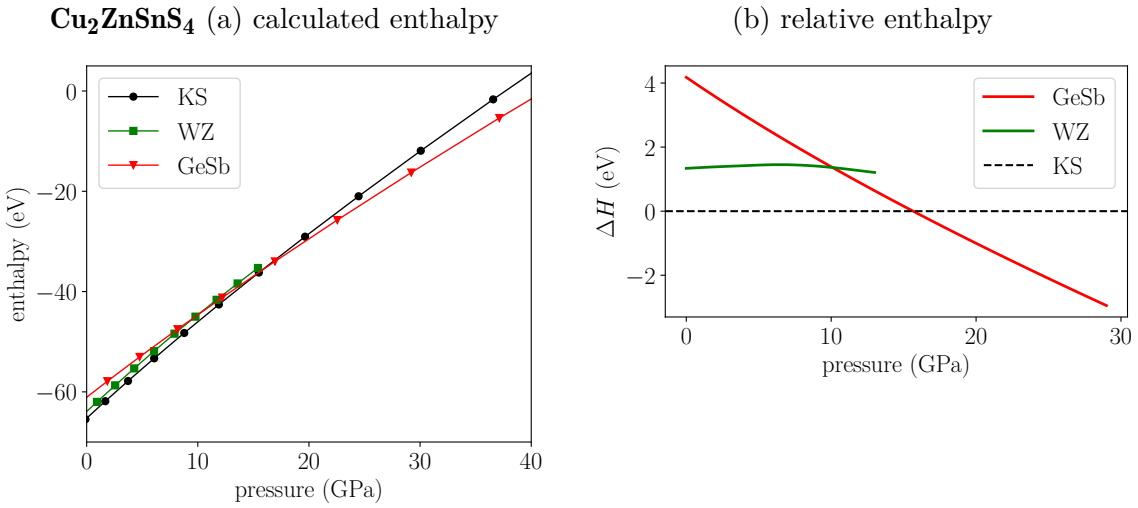

Figure 4.4: (a) Calculated PBE enthalpies for KS, WZ and GeSb-type structural models as a function of pressure for Cu_2ZnSnS_4. Because the enthalpy differences are very small we also calculated relative enthalpy differences (b) with reference to the KS structure.

The PBE prediction agrees well with the experimental XRD results. The XRD reflexes (fig. 4.5a) indicate a transition in the range from 14 to 16 GPa. The experimental lattice constants (fig. 4.5b) show a discontinuity at 15 GPa related to the phase transition from KS to GeSb-type.

The PBE lattice parameters of the low and high-pressure phase are close to the experimental results. Only the lattice constant c of KS is noticeably overestimated by PBE.

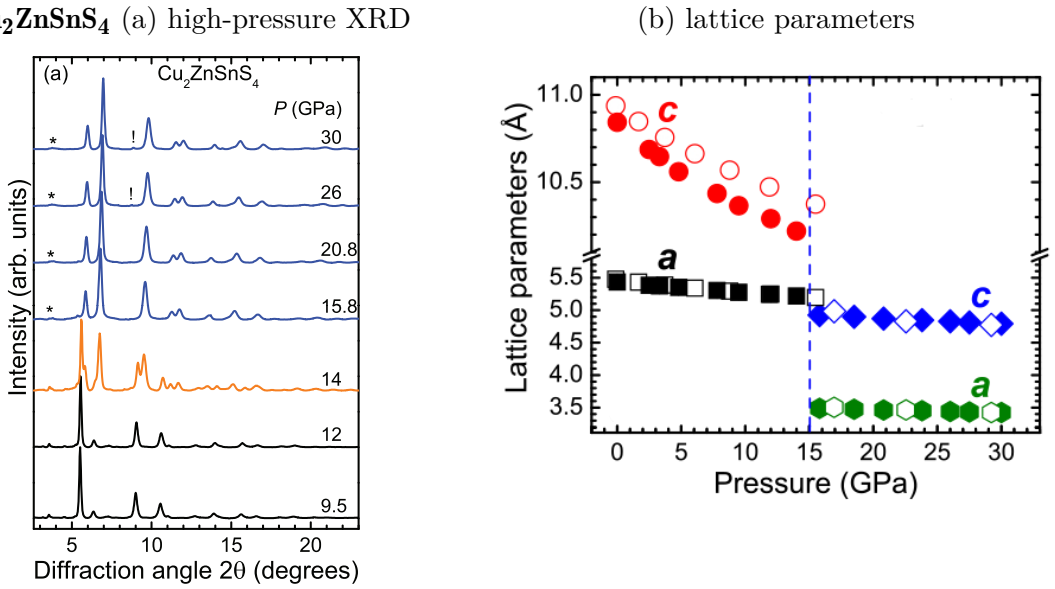

Figure 4.5: (a) high-pressure XRD reflexes for Cu_2ZnSnS_4. The pattern of KS is depicted in black, the pattern of GeSb-type is depicted in blue and the mixed signal is shown in orange. (b) Lattice parameter evolution (a and c) with respect to the pressure, filled symbols are experimental data and the open symbols are the PBE predictions.

The experimental and theoretical results for DKS (**paper B**) are very similar to KS. In a high-pressure XRD experiment a DKS to GeSb-type transition is observed around 15 GPa. The PBE transition is again predicted at 16 GPa. The disorder has no influence on the transition pressure. At the PBE level that can be explained with the similarity of the used DKS and KS structure. We see evidence that the DKS model is not as close to the experimental structure as for the ordered KS case. The Birch–Murnaghan fit parameter vary significantly between PBE and the experiment (tab. 4.2). For ideal KS that is not the case; the fit parameter agree closely.

Table 4.2: Fitted parameter for the Birch–Murnaghan equation of state for Cu_2ZnSnS_4. B_0 (in GPa): bulk modulus at zero pressure, V_0/Z (in Å^3): reference volume per f.u. at equilibrium and $B_0^{'}$: pressure derivative of the bulk modulus at zero pressure.

Structure	method	V_0/Z	B_0	$B_0^{'}$	source
KS	exp.	160.1	74	4.4	**paper A**
	PBE	163.7	68.6	4.6	
DKS	exp.	162.3	43	11	**paper B**
	PBE	163.7	68.7	4.6	

Our calculations for the materials Ag_2ZnSnS_4, Ag_2CdSnS_4, Cu_2FeSnS_4 and Cu_2MnSnS_4 are the first predictions for the high-pressure phase transitions. There is no experimental reference

data available yet. Therefore we will describe the results by themselves and compare to CZTS. For Ag_2ZnSnS_4 PBE predicts a transition from KS to GeSb at 8.2 GPa, so only half the transition pressure of CZTS (tab. 4.3). Additionally replacing Zn by Cd reduces the transition pressure again nearly by a factor of 2. As the equilibrium phase for Ag_2ZnSnS_4 can not be unambiguously determined at the PBE level. We can not predict if we expect a WZ-KS or KS to GeSb transition. We lean towards the WZ-KS equilibrium phase based on the fact that it has been observed experimentally at room temperature and ambient pressure.[77] In Cu_2FeSnS_4 we observe a structural transition from $P\bar{4}$ to GeSb-type at 16.3 GPa. The transition pressure is nearly identical to the pressure for CZTS. The magnetic phase of GeSb-type Cu_2FeSnS_4 remains antiferromagnetic up to 23.0 GPa when it flips to ferromagnetic. In Cu_2MnSnS_4 the transition pressure is slightly reduced in comparison to CZTS. We predict a KS to GeSb-type transition at 12.1 GPa. Interestingly in this case the magnetic phase changes simultaneously from anti-ferromagnetic to ferromagnetic.

Table 4.3: Predicted transitions for Ag_2ZnSnS_4, Ag_2CdSnS_4, Cu_2FeSnS_4 and Cu_2MnSnS_4 in comparison to transition for Cu_2ZnSnS_4. The table contains the transition pressure (p_T in GPa, if available the experimental p_T is given in parenthesis) with the corresponding cell volumes before (V_1 in Å^3) and after (V_2 in Å^3) the transition, ΔV denotes the relative volume change. The volumina all refer to the KS unit cell size, for the $P\bar{4}$ and GeSb-type structures that refers to two unit cells.

Composition	p_T (exp.)	transition	V_1	V_2	ΔV	**paper**
Cu_2ZnSnS_4	16.0 (≈15)	KS → GeSb	280	240	-15.2 %	**A**
Cu_2ZnSnS_4	16.0 (≈15)	DKS → GeSb	280	240	-15.2 %	**B**
Ag_2ZnSnS_4	8.2	KS → GeSb	337	282	-16.3 %	**C**
Ag_2CdSnS_4	4.7	WZ-KS/KS → GeSb	374	306	-18.0 %	**C**
Cu_2FeSnS_4	16.3	$P\bar{4}$(AM) → GeSb(AM)	272	236	-13.1 %	**D**
Cu_2FeSnS_4	23.0	GeSb(AM) → GeSb(FM)	226	225	-0.6 %	**D**
Cu_2MnSnS_4	12.1	KS(AM) → GeSb(FM)	289	248	-14.0 %	**D**

Although the equilibrium structures of the investigated materials slightly differ we can understand the changes in the transition pressures based on the ionic radii[39] of the cations. For CZTS they are: r(Cu^+)=0.60 Å, r(Zn^{2+})=0.60 Å and r(Sn^{4+})=0.55 Å. In this material all cations have a similar radius and it is the most stable material against pressure together with Cu_2FeSnS_4. The ionic radii of Fe (r(Fe^{2+})=0.63 Å) and Zn^{2+} are similar and we conclude hence the similar transition pressure. Mn (r(Mn^{2+})=0.66 Å) has a slightly larger ionic radius than Fe and Zn and the transition pressure is reduced by 25%. In Ag_2ZnSnS_4 the radius of the univalent cation is increase significantly (r(Ag^+)=1.00 Å), which we suspect can explain the drop in transition pressure by 50%. Additionally also replacing Zn by Cd (r(Cd^{2+})=0.78 Å) further increase the imbalance in the cation size, which once more reduces the transition pressure.

To fully understand the consequences of the predicted high-pressure transition for the use as solar cell absorbers we need to analyze the impact of the transition on the electronic structure. We calculated the DOS (density of states) before and after the transition at the HSE06 level

using the PBE structures. For Cu_2ZnSnS_4 we found that the KS band gap widens from the equilibrium value of 1.2 eV to 2.1 eV at the transition pressure (fig. 4.6 left). After the transition to GeSb the DOS changed drastically, and the material is no longer semi-conducting but metallic (fig. 4.6 right). The metallic character has been confirmed experimentally by UV/vis measurements.

Composition	p_T in GPa	DOS_1	DOS_2	E_g in eV
Cu_2ZnSnS_4	16.0	KS	GeSb	$2.1 \rightarrow 0.0$

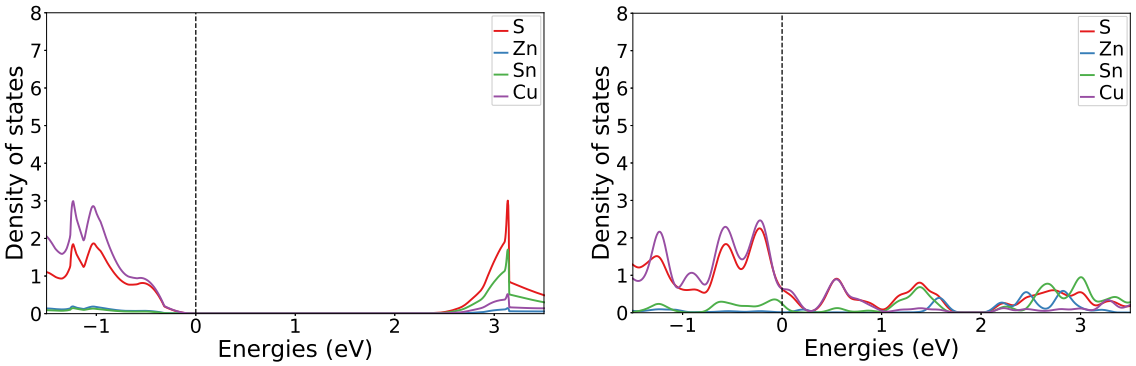

Figure 4.6: DOS plots at the transition pressure at the HSE06 level for KS and GeSb-type Cu_2ZnSnS_4.

The situation for all other materials is identical. Prior to the transition the band gap widens and afterwards the GeSb phase is metallic. That means if the pressure induced transitions are triggered all studied materials are rendered useless as a solar cell absorbers. The transition presents a hard physical limitation for the application. All transition pressures except for the pressure for Ag_2CdSnS_4 are well beyond 3 GPa which is the maximum we expect in thin-film processing. Consequently we do not see an issue with using those materials in thin-film solar cells. For Ag_2CdSnS_4 the transition pressure of 4.7 GPa is not far off the maximum pressure we expect in thin-films and we think that this could lead to performance problems and advice to monitor the structure closely for this material if used as an absorber material.

Another aspect we studied exclusively for Ag_2ZnSnS_4 and Ag_2CdSnS_4 (**paper C**) is KS disorder. In CZTS one of the recognized issues is Cu-Zn disorder [2,40] in the planes they share (fig. 4.2a). The main reason why Cu^+ (ionic radius: 0.60 Å) and Zn^{2+} (ionic radius: 0.60 Å) can be interchanged easily are their similar ionic radii. [39] Although Ag_2CdSnS_4 has a WZ-KS equilibrium structure we investigate the disorder in the KS structure which is only 22 meV less stable. This can give an indication how (partly) substituting KS Cu_2ZnSnS_4 with Ag and Cd together [82] influences disorder. We classify disordered structures by their disorder fraction, which we define as the number of atoms in the two Cu-Zn planes within the cell which have changed their place in comparison to the fully ordered KS structure divided by the total number of atoms of the planes. In the kesterite unit cell (fig. 4.1a) there are four atoms within the two Cu-Zn planes. Exchanging two of them leads to a disorder fraction of 50 % (fig. 4.2b). Disorder fractions above 50 % lead to the same structures as for the disorder

fractions below due to the crystal symmetry. In a previous study in our group we calculated all possible disorder patterns for CZTS in 2x2x1 super cells.[41] In this study we picked three representative disorder patterns for each disorder fraction. We chose a pattern with a high, medium and low energy of formation for each disorder fraction. We optimized each disorder pattern for Ag_2ZnSnS_4 and Ag_2CdSnS_4 (fig. 4.7a and b) to analyze how the energies of the disordered structures compare to the energies in CZTS (fig. 4.7c).

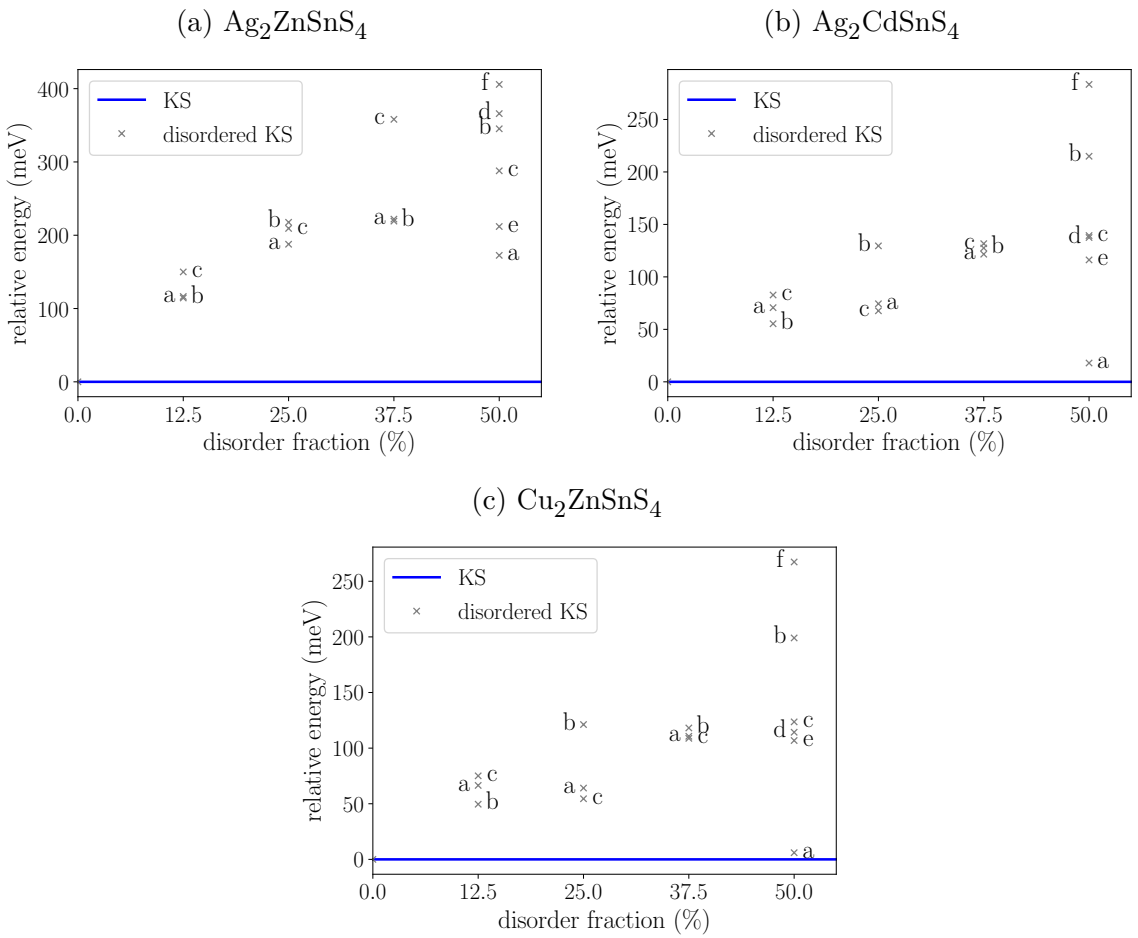

Figure 4.7: Relative PBE energies of disordered KS structures with reference to ideal KS for a) Ag_2ZnSnS_4, b) Ag_2CdSnS_4 and c) Cu_2ZnSnS_4.[2]

In Ag_2ZnSnS_4 the disordered structures are destabilized by about 50-100 meV in comparison to CZTS. Importantly the disorder pattern (a) which corresponds to the $P\bar{4}2c$ symmetric DKS structure (fig. 4.2b) is 170 meV less stable than in CZTS. In CZTS this pattern is nearly as stable as KS and we suspect that the existence of this structure is one if the main reason why CZTS is sensitive to disorder. The situation in Ag_2CdSnS_4 is different than in Ag_2ZnSnS_4, the energies of the disordered structures including pattern (a) are very similar to the values in CZTS. We conclude that Ag_2ZnSnS_4 is less sensitive to disorder than CZTS while Ag_2CdSnS_4 is similarly sensitive to disorder as CZTS.

We think that the reason is that the ionic radii of Cu^{+} ($r(Cu^{+})$=0.60 Å) and Zn^{2+} ($r(Zn^{2+})$=0.60 Å) are relatively similar as well as the ionic radii of Ag^{+} ($r(Ag^{+})$=1.00 Å) and Cd^{2+} ($r(Cd^{2+})$=0.78 Å). Those elements constitute two planes in the KS unit cell which can easily get disordered if the elements are similar in size. In Ag_2ZnSnS_4 the effective ionic radii of the elements are sufficiently different for the disordered structures to be destabilized in comparison to Cu_2ZnSnS_4 and Ag_2CdSnS_4.

Similarly to Cu_2MnSnS_4 and Cu_2FeSnS_4 the Cd-substituted CZTS variant Cu_2CdSnS_4 does not have a KS equilibrium structure. As explained above this raises the question how much substitution in CZTS is possible without losing the desired KS structure. The **paper E** answers this question by investigating the solid solution series $Cu_2Zn_{1-x}Cd_xSnS_4$. The end members Cu_2ZnSnS_4 and Cu_2CdSnS_4 crystallize in KS (fig. 4.1a) and ST (fig. 4.1d) structure, respectively. We investigated at which cadmium substitution fraction x_{Cd} the structure flips from KS to ST. Our collaborators synthesized samples with different x_{Cd} ranging from 0 to 1. They measured the XRD reflexes to determined when the structure changes. We generate 2x2x1 super cells of KS and ST with 64 atoms (8 Zn) then we stepwise replace the Zn, only considering symmetry inequivalent substitution patterns. We optimize each substitution pattern at the PBE level. Next we average the energies for each x_{Cd} and then compare KS and ST to find x_{Cd} where the ST structure becomes more stable. Because disorder is common in CZTS we also included two disordered structures, one with 12.5 % and one with 50 % disorder (fig. 4.8). The aim is to understand how the transition is affected by increasing disorder in the KS phase.

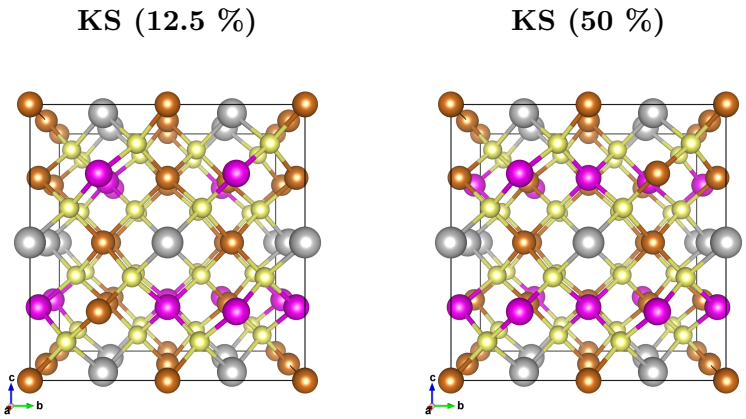

Figure 4.8: Tested disordered kesterite structures. The number in parenthesis refers to the disorder fraction. Copper: Cu, pink: Zn, grey: Sn and yellow: S.

To visualize the transition we plot the averaged (disordered) KS PBE energies with reference to the averaged PBE energies for the ST phase (fig. 4.9). The trend for ideal KS increases from 0 to 1. At 0.51 x_{Cd} KS becomes less stable than ST. Our experimental colleagues observed the transition already at 0.40 x_{Cd}, which we consider a good agreement with our PBE prediction.

We also compared the lattice parameter between PBE and the experiment and found that they are within the expected error for the PBE functional for all structures and substitution fractions.

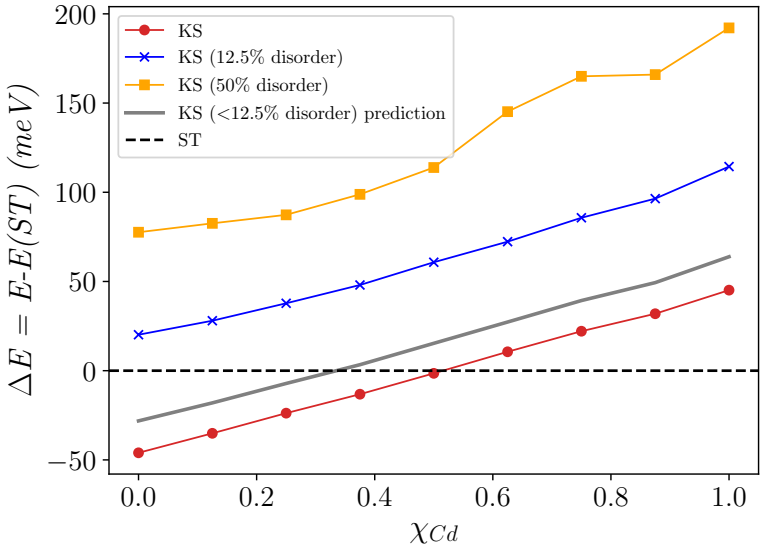

Figure 4.9: Relative energy of the kesterite phases (solid lines) with respect to the stannite phase (black dotted baseline) for different Cd substitution fractions. Energies below zero means the KS phase is more stable.

The trend for the disordered phases shows that KS is destabilized with increasing disorder. We concluded that part of the deviation between PBE and experiment could be due to the KS samples containing a small disorder (much smaller than 12.5%). In the plot (fig. 4.8) we included a grey line to illustrate what trend we would expect for this kind of disordered structure. We also calculated the HSE06 band gaps for the most stable substitution pattern at each x_{Cd} and they agree well with experimental data, also hinting that the experimental sample may be slightly disordered.

The material properties of kesterites are in principle very suitable for solar cell absorbers but so far the synthesis and processing of the cells is not yet at a level that they can convert that to high performing solar cells. In particular the high V_{OC} deficit remains a big challenge which has to be overcome for kesterite solar cells to become commercially relevant. One promising way to achieve that is cationic substitution. In this work we have shown that there is no issue with using CZTS absorbers in thin-films in terms of structural integrity against pressures expected in thin-films. Based on our results we think the same holds for Ag, Cd, Mn and Fe substituted CZTS. Only when simultaneously doping with Ag and Cd we advice caution because the transition pressure to a metallic high-pressure phase is particularly low for Ag_2CdSnS_4.

Carrying out high-pressure XRD experiments requires a lot of time and effort. In this thesis we have shown that for CZTS the prediction of the transition pressures using PBE works well yielding similar results as the XRD experiments. Also the electronic properties calculated with the HSE06 functional agree well with experimental data. We conclude that first principle calculation are a valuable tool to asses high-pressure phase transitions. We recommend to use it prior to carrying out experimental XRD studies to screen for materials which are sufficiently pressure resistant. This enables experimentalist to focus their efforts on materials which are suitable for the use in thin-film solar cells.

Bibliography

[1] D. E. Carlson, C. R. Wronski, *Applied Physics Letters* **1976**, *28*(11), 671–673.

[2] M. Quennet, A. Ritscher, M. Lerch, B. Paulus, *Journal of Solid State Chemistry* **2017**, *250*(January), er.

[3] U. N. D. Programme, W. E. Council, Energy and the challenge of sustainability.

[4] S. A. Khalate, R. S. Kate, R. J. Deokate, *Solar Energy* **2018**, *169*(May), 616–633.

[5] W. Shockley, H. J. Queisser, *Journal of Applied Physics* **1961**, *32*(3), 510–519.

[6] D. N. Congreve, J. Lee, N. J. Thompson, E. Hontz, S. R. Yost, P. D. Reusswig, M. E. Bahlke, S. Reineke, T. Van Voorhis, M. A. Baldo, *Science* **2013**, *340*(6130), 334–337.

[7] M. Green, E. Dunlop, J. Hohl-Ebinger, M. Yoshita, N. Kopidakis, X. Hao, *Progress in Photovoltaics: Research and Applications* **2021**, *29*(1), 3–15.

[8] P. Würfel, *Physics of solar cells : from basic principles to advanced concepts / Peter Würfel and Uli Würfel.*, 3. Aufl., **2016**.

[9] T. D. Lee, A. U. Ebong, *Renewable and Sustainable Energy Reviews* **2017**, *70*(September 2015), 1286–1297.

[10] H. Sai, T. Matsui, K. Matsubara, *Applied Physics Letters* **2016**, *109*(18), 1–6.

[11] C. Ferekides, J. Britt, Y. Ma, L. Killian, *Conference Record of the IEEE Photovoltaic Specialists Conference* **1993**, 389–393.

[12] X. Liu, Y. Feng, H. Cui, F. Liu, X. Hao, G. Conibeer, D. B. Mitzi, M. Green, *Progress in Photovoltaics: Research and Applications* **2016**, *24*(6), 879–898.

[13] H. Katagiri, N. Sasaguchi, S. Hando, S. Hoshino, J. Ohashi, T. Yokota, *Solar Energy Materials and Solar Cells* **1997**, *49*(1-4), 407–414.

[14] S. Schorr, *Solar Energy Materials and Solar Cells* **2011**, *95*(6), 1482–1488.

[15] S. Siebentritt, S. Schorr, *Progress in Photovoltaics: Research and Applications* **2012**, *20*(5), 512–519.

[16] J. J. Scragg, P. J. Dale, L. M. Peter, G. Zoppi, I. Forbes, *Physica Status Solidi (B) Basic Research* **2008**, *245*(9), 1772–1778.

[17] S. Giraldo, Z. Jehl, M. Placidi, V. Izquierdo-Roca, A. Pérez-Rodríguez, E. Saucedo, *Advanced Materials* **2019**, *31*(16), 1806692.

[18] H. Wei, Z. Ye, M. Li, Y. Su, Z. Yang, Y. Zhang, *CrystEngComm* **2011**, *13*(7), 2222–2226.

[19] T. J. Huang, X. Yin, G. Qi, H. Gong, *Physica Status Solidi - Rapid Research Letters* **2014**, *8*(9), 735–762.

[20] Z. Shi, D. Attygalle, A. H. Jayatissa, *Journal of Materials Science: Materials in Electronics* **2017**, *28*(2), 2290–2306.

[21] W. Wang, M. T. Winkler, O. Gunawan, T. Gokmen, T. K. Todorov, Y. Zhu, D. B. Mitzi, *Advanced Energy Materials* **2014**, *4*(7), 1–5.

[22] A. Lafond, L. Choubrac, C. Guillot-Deudon, P. Deniard, S. Jobic, *Zeitschrift fur Anorganische und Allgemeine Chemie* **2012**, *638*(15), 2571–2577.

[23] G. Gurieva, R. Ferreira, P. Knoll, S. Schorr, *Physica Status Solidi (A) Applications and Materials Science* **2018**, *215*(17), 4–9.

[24] M. Dimitrievska, A. Fairbrother, E. Saucedo, A. Pérez-Rodríguez, V. Izquierdo-Roca, *Solar Energy Materials and Solar Cells* **2016**, *149*, 304–309.

[25] S. Chen, J. H. Yang, X. G. Gong, A. Walsh, S. H. Wei, *Physical Review B - Condensed Matter and Materials Physics* **2010**, *81*(24), 35–37.

[26] J. Márquez, M. Neuschitzer, M. Dimitrievska, R. Gunder, S. Haass, M. Werner, Y. E. Romanyuk, S. Schorr, N. M. Pearsall, I. Forbes, *Solar Energy Materials and Solar Cells* **2016**, *144*, 579–585.

[27] Y. S. Lee, T. Gershon, O. Gunawan, T. K. Todorov, T. Gokmen, Y. Virgus, S. Guha, *Advanced Energy Materials* **2015**, *5*(7), 2–5.

[28] L. Vauche, L. Risch, Y. Sánchez, M. Dimitrievska, M. Pasquinelli, T. Goislard de Monsabert, P.-P. Grand, S. Jaime-Ferrer, E. Saucedo, *Progress in Photovoltaics: Research and Applications* **2016**, *24*(1), 38–51.

[29] K. Timmo, M. Altosaar, J. Raudoja, K. Muska, M. Pilvet, M. Kauk, T. Varema, M. Danilson, O. Volobujeva, E. Mellikov, *Solar Energy Materials and Solar Cells* **2010**, *94*(11), 1889–1892.

[30] A. Ritscher, J. Just, O. Dolotko, S. Schorr, M. Lerch, *Journal of Alloys and Compounds* **2016**, *670*, 289–296.

[31] G. S. Babu, Y. B. Kumar, P. U. Bhaskar, V. S. Raja, *Semiconductor Science and Technology* **2008**, *23*(8), 085023.

[32] P. Jackson, D. Hariskos, E. Lotter, S. Paetel, R. Wuerz, R. Menner, W. Wischmann, M. Powalla, *Progress in Photovoltaics: Research and Applications* **2011**, *19*(7), 894–897.

[33] R. Haight, A. Barkhouse, O. Gunawan, B. Shin, M. Copel, M. Hopstaken, D. B. Mitzi, *Applied Physics Letters* **2011**, *98*(25).

[34] M. Bär, B. A. Schubert, B. Marsen, R. G. Wilks, S. Pookpanratana, M. Blum, S. Krause, T. Unold, W. Yang, L. Weinhardt, C. Heske, H. W. Schock, *Applied Physics Letters* **2011**, *99*(22), 2011–2014.

[35] D. A. R. Barkhouse, R. Haight, N. Sakai, H. Hiroi, H. Sugimoto, D. B. Mitzi, *Applied Physics Letters* **2012**, *100*(19), 4–9.

[36] J. F. Wager, *AIP Advances* **2017**, *7*(12).

[37] T. Gokmen, O. Gunawan, T. K. Todorov, D. B. Mitzi, *Applied Physics Letters* **2013**, *103*(10), 2–7.

[38] S. Bourdais, C. Choné, B. Delatouche, A. Jacob, G. Larramona, C. Moisan, A. Lafond, F. Donatini, G. Rey, S. Siebentritt, A. Walsh, G. Dennler, *Advanced Energy Materials* **2016**, *6*(12).

[39] R. D. Shannon, *Acta Crystallographica Section A* **1976**, *32*(5), 751–767.

[40] J. J. S. Scragg, J. K. Larsen, M. Kumar, C. Persson, J. Sendler, S. Siebentritt, C. Platzer Björkman, *Physica Status Solidi (B) Basic Research* **2016**, *253*(2), 247–254.

[41] Marcel Quennet, Dissertation, Freie Universität Berlin, **2016**.

[42] A. Mule, B. Vermang, M. Sylvester, G. Brammertz, S. Ranjbar, T. Schnabel, N. Gampa, M. Meuris, J. Poortmans, *Thin Solid Films* **2017**, *633*, 156–161.

[43] G. C. Janssen, *Thin Solid Films* **2007**, *515*(17), 6654–6664.

[44] P. Taylor, V. Presser, K. G. Nickel, *Crtitical Reviews in Solid State and Matrials Sciences* **2008**, (March 2013), 37–41.

[45] T. Tanaka, T. Nagatomo, D. Kawasaki, M. Nishio, Q. Guo, A. Wakahara, A. Yoshida, H. Ogawa, *Journal of Physics and Chemistry of Solids* **2005**, *66*(11), 1978–1981.

[46] J. P. Perdew, K. Burke, M. Ernzerhof, *Physical Review Letters* **1996**, *77*(18), 3865–3868.

[47] J. Heyd, G. E. Scuseria, M. Ernzerhof, *Journal of Chemical Physics* **2003**, *118*(18), 8207–8215.

[48] E. Schrödinger, *Physical Review* **1926**, *28*(6), 1049–1070.

[49] M. Born, R. Oppenheimer, *Annalen der Physik* **1927**, *389*(20), 457–484.

[50] J. C. Slater, *Physical Review* **1929**, *34*(10), 1293–1322.

[51] W. Pauli, *Zeitschrift für Physik* **1925**, *31*(1), 765–783.

[52] C. C. Roothaan, *Reviews of Modern Physics* **1951**, *23*(2), 69–89.

[53] G. G. Hall, P. R. S. L. A, *Proceedings of the Royal Society of London. Series A. Mathematical and Physical Sciences* **1951**, *205*(1083), 541–552.

[54] V. Fock, *Zeitschrift für Physik* **1930**, *61*(1-2), 126–148.

[55] C. J. Cramer, *Essentials of Computational Chemistry: Theories and Models*, 2. Aufl., Wiley, New York, **2005**.

[56] P. Hohenberg, W. Kohn, *Physical Review* **1964**, *136*(3B), B864–B871.

[57] W. Kohn, L. J. Sham, *Physical Review* **1965**, *140*(4A), A1133–A1138.

[58] R. G. Parr, W. Yang, *Density functional theory of atoms and molecules*, «The» international series of monographs on chemistry 16, Oxford Univ. Press, New York, **1989**.

[59] A. D. Becke, *Physical Review A* **1988**, *38*(6), 3098–3100.

[60] J. P. Perdew, J. A. Chevary, S. H. Vosko, K. A. Jackson, M. R. Pederson, D. J. Singh, C. Fiolhais, *Physical Review B* **1992**, *46*(11), 6671–6687.

[61] C. Lee, W. Yang, R. G. Parr, *Physical Review B* **1988**, *37*(2), 785–789.

[62] J. P. Perdew, *Physical Review B* **1986**, *33*(12), 8822–8824.

[63] C. Adamo, V. Barone, *The Journal of Chemical Physics* **1999**, *110*(13), 6158–6170.

[64] J. M. Crowley, J. Tahir-Kheli, W. A. Goddard, *Journal of Physical Chemistry Letters* **2016**, *7*(7), 1198–1203.

[65] N. W. Ashcroft, N. D. Mermin, S. Rodriguez, *American Journal of Physics* **1978**, *46*(1), 116–117.

[66] F. Bloch, *Zeitschrift für Physik* **1929**, *52*(7-8), 555–600.

[67] L. de Broglie, *Foundations of Physics* **1970**, *1*(1), 5–15.

[68] H. J. Monkhorst, J. D. Pack, *Physical Review B* **1976**, *13*(12), 5188–5192.

[69] J. G. Hill, *International Journal of Quantum Chemistry* **2013**, *113*(1), 21–34.

[70] B. Silvi, M. Causà, R. Dovesi, C. Roetti, *Molecular Physics* **1989**, *67*(4), 891–901.

[71] R. Dronskowski, *Computational chemistry of solid state materials : a guide for materials scientists, chemists, physicists and others / Richard Dronskowski*, Weinheim, **2005**.

[72] P. E. Blöchl, *Physical Review B* **1994**, *50*(24), 17953–17979.

[73] G. Kresse, D. Joubert, *Physical Review B* **1999**, *59*(3), 1758–1775.

[74] F. Birch, *Physical Review* **1947**, *71*(11), 809–824.

[75] G. X. Zhang, A. M. Reilly, A. Tkatchenko, M. Scheffler, *New Journal of Physics* **2018**, *20*(6).

[76] P. Mangelis, A. Aziz, I. Da Silva, R. Grau-Crespo, P. Vaqueiro, A. V. Powell, *Physical Chemistry Chemical Physics* **2019**, *21*(35), 19311–19317.

[77] E. M. Heppke, S. Berendts, M. Lerch, *Zeitschrift für Naturforschung B* **2020**, *75*(4), 393–402.

[78] C. Rincón, M. Quintero, E. Moreno, C. Power, E. Quintero, J. A. Henao, M. A. MacÍas, G. E. Delgado, R. Tovar, M. Morocoima, *Solid State Communications* **2011**, *151*(13), 947–951.

[79] T. Fries, Y. Shapira, F. Palacio, M. C. Morón, *Physical Review B - Condensed Matter and Materials Physics* **1997**, *56*(9), 5424–5431.

[80] T. Shibuya, Y. Goto, Y. Kamihara, M. Matoba, K. Yasuoka, L. A. Burton, A. Walsh, *Applied Physics Letters* **2014**, *104*(2).

[81] P. Ramavath, P. Biswas, R. S. Kumar, V. Mahendar, G. V. Rao, U. S. Hareesh, R. Johnson, N. E. Prasad, *Ceramics International* **2011**, *37*(3), 1039–1046.

[82] T. Gershon, Y. S. Lee, P. Antunez, R. Mankad, S. Singh, D. Bishop, O. Gunawan, M. Hopstaken, R. Haight, *Advanced Energy Materials* **2016**, *6*(10), 1–7.